Summer 2009

Practical localized waves generation

Mohamed Ahmed Salem
New Jersey Institute of Technology

ABSTRACT

PRACTICAL LOCALIZED WAVES GENERATION

by
Mohamed Ahmed Salem

Since the early works on localized waves (LW), extensive results were published on this important subject, from both the theoretical and the experimental points of view. Nevertheless, those experimental techniques of LW generation suffer from several shortcomings. A major one is that only pulse peaks were accredited. Either the full profile of the generated pulse was not reported, or it was not closely matching the theoretical profile. Additionally, low resolutions of the generated LWs were reported in the acoustic X-Waves. The conductors of the experiment attributed this effect to the limited bandwidth of the excitation elements.

The interest in the unique features of LWs and their high potential in different applications were the main motivation for conducting this study. Because of the complex nature of LWs, it is challenging to design a system that can launch LWs with high accuracy and power efficiency as well as the flexibility in choosing the LWs design parameters. Due to practical limitations, the results of this research could not yet be experimentally verified; however, this research aims to provide a practically feasible method for LWs generation that avoids the shortcomings of previous techniques.

In the study, the transverse electric (TE) version of the MPS pulse is derived. Expansion in terms of the waveguide's orthogonal modes is presented and followed by the method to determine the excitation currents for the loop antennas inside a circular waveguide. The feasibility and flexibility of the method is demonstrated via numerical examples.

PRACTICAL LOCALIZED WAVES GENERATION

by
Mohamed Ahmed Salem

A Dissertation
Submitted to the Faculty of
New Jersey Institute of Technology
in Partial Fulfillment of the Requirements for the Degree of
Doctor of Philosophy in Electrical Engineering

Department of Electrical and Computer Engineering

August 2009

APPROVAL PAGE

PRACTICAL LOCALIZED WAVES GENERATION

Mohamed Ahmed Salem

Dr. Edip Niver, Dissertation Advisor Professor of Electrical and Computer Engineering, NJIT	Date
Dr. Gerald Whitman, Committee Member Professor of Electrical and Computer Engineering, NJIT	Date
Dr. Haim Grebel, Committee Member Professor of Electrical and Computer Engineering, NJIT	Date
Dr. Gregory A. Kriegsmann, Committee Member Distinguished Professor of Mathematics, NJIT	Date
Dr. Richard V. Snyder, Committee Member President of RS Microwave Company, Inc., Butler, NJ	Date

BIOGRAPHICAL SKETCH

Author: Mohamed Ahmed Salem

Degree: Doctor of Philosophy

Date: August 2009

Undergraduate and Graduate Education:

- Doctor of Philosophy in Electrical Engineering,
  New Jersey Institute of Technology, Newark, NJ, 2009

- Master of Science in Electrical Engineering,
  Ain Shams University, Cairo, Egypt, 2004

- Bachelor of Science in Electrical Engineering,
  Ain Shams University, Cairo, Egypt, 2001

Major: Electrical Engineering

Patent Applications:

E. Niver, M. Salem and A. Kamel, "*Multimode Excitation of Short Pulse Launchers to Generate Localized Waves*," Patent application in progress. May 2009.

"O my Lord! Advance me in knowledge"
-Holy Qur'an 20:114

ACKNOWLEDGMENT

I would like to express my deepest appreciation to Dr. Edip Niver, who not only served as my research supervisor, providing valuable and countless resources, insight, and intuition, but also constantly gave me support, encouragement, and reassurance. Special thanks are given to Dr. Gerald Whitman, Dr. Haim Grebel, Dr. Gregory A. Kriegsmann and Dr. Richard V. Snyder for actively participating in my committee.

I also wish to thank Nedime Pelin Yalcin and Oksana Manzhura for their assistance and friendship during the course of my study. Finally, I would like to express my deep gratitude to all my family members for their love and support.

TABLE OF CONTENTS

TABLE OF CONTENTS
(Continued)

LIST OF TABLES

LIST OF FIGURES

LIST OF FIGURES
(Continued)

LIST OF FIGURES
(Continued)

Figure **Page**

CHAPTER 1

INTRODUCTION

1.1 Objective

The objective of this dissertation is to present a novel method for localized waves (LW's) generation in the microwave regime.

Because of the scalar nature of the LW solutions, first the electromagnetic transverse electric (TE) vector formulation is derived and its main physical properties are mapped to the mathematical parameters of the localized waves.

The method utilizes the completeness and orthogonality properties of the propagating modes of cylindrical metallic waveguides to decompose the localized waves. The localized wave field is matched to the aperture field at the waveguide's open end and the incident field and the modal excitation coefficients are then determined.

Excitation of the corresponding waveguide's modes is accomplished by means of circular current loops placed inside of the waveguide. A linear system is formed to map the unknown current loops excitation currents to the modes excitation coefficients, thus by solving this system the unknown currents are found.

The study aims to provide a flexible yet systematic physically realizable method to generate localized waves that is also feasible for commercial and industrial implementation.

1.2 Historical Overview

The early work of Brittingham [1] in 1983 led to the discovery of a slow-decaying and non-dispersing class of exact Maxwell's equations solutions. The original solution was termed focus waves modes (FWMs) and is structured on 3D pulses that carry energy with the speed of light along linear paths. Brittingham introduced two surfaces of discontinuity to render the FWM finite in terms of energy; however Wu and King [2] proved that the discontinuous solution does not satisfy Maxwell's equations. Sezginer [3] and Wu and Lehmann [4] proved that any finite energy solutions will result in dispersion and loss of energy.

In 1985, Ziolkowski [5] showed that the superposition of FWMs results in finite energy and slow-decaying solutions, which are characterized by their high directivity, hence termed directed energy pulse trains (DEPTs).

Lu and Greenleaf [6] introduced another class of non-diffracting solutions to Maxwell's equations that are termed X-Waves due to their shape in the plane through their axes. X-Waves travel to infinity without spreading provided that they are generated from infinite apertures. This family of solutions has an infinite total energy but finite energy density.

Several types of localized solutions were introduced in the literature over the years [7-15]; however, due to the difficulty in practically generating them, most of the presented work was purely theoretical. Additionally, most of the initial practical work done on localized waves was conducted in the acoustic domain [9-11] because of the scalar nature of the solutions.

1.3 Characteristics and Application Potential of Localized Waves

Localized waves are solutions to the homogenous scalar wave equation. The most notable characteristics of LWs are:

- Ultra-wideband compact in space and time pulses in sparse background.
- Non-separable spatio-temporal functions.
- Ideally propagate without diffraction or with only local deformations for infinite distances.

While some types of the LW solutions permit superluminal propagation velocities, it is to be noted that this does not violate the theory of special relativity and thus no superluminal information transfer takes place [16]-[17].

The aforementioned characteristics promote their high potential in the following applications:

- Remote sensing.
- High-resolution imaging.
- Medical radiology and tissue characterization.
- Non-destructive testing.
- Directed energy transfer.
- Secure communication.
- Impulse radar.
- Electronic warfare.

1.4 Spectral Structure of Localized Waves

To understand the concept of the non-diffracting waves, it is necessary to establish precise mathematical definition of these solutions. Such mathematical concepts are essential to extract the necessary spectral structure of the non-diffracting waves.

Intuitively, an ideal non-diffracting wave, whether a beam or a pulse, can be defined as a wave capable of maintaining its spatial form indefinitely while propagating. Local variations are excluded from the former definition. This property could be mathematically expressed as

$$\Psi(\rho,\varphi,z,t)=\Psi\left(\rho,\varphi,z+\Delta z_0,t+\frac{\Delta z_0}{V}\right) \tag{1.1}$$

where $\Psi(\rho,\varphi,z,t)$ is the wave function in the cylindrical coordinates (ρ,φ,z), t is the time variable, Δz_0 is a certain distance and V is the propagation speed of the wave.

Using the Fourier-Bessel expansion, the wave function could be expressed as

$$\Psi(\rho,\varphi,z,t)=\sum_{n=-\infty}^{\infty}\left[\int_{-\infty}^{\infty}\int_{-\infty}^{\infty}\int_{0}^{\infty}S_n(k_\rho,k_z,\omega)J_n(k_\rho\rho)e^{i(k_z z-\omega t)}e^{in\varphi}k_\rho dk_\rho dk_z d\omega\right], \tag{1.2}$$

with $S_n(k_\rho,k_z,\omega)$ being the n-th component of the wave's spectrum, $J_n(\cdot)$ is the standard cylindrical Bessel function of first kind and order n, (k_ρ,k_z,ω) are the transformed spectral variables of (ρ,z,t), respectively, with $\omega^2/c^2=k_\rho^2+k_z^2$ and c is the speed of light in vacuum. On using the translation property of the Fourier transform, $T[f(x+a)]=e^{ika}T[f(x)]$, the Fourier-Bessel transforms of the left-hand side and right-hand side of equation (1.1) are $S_n(k_\rho,k_z,\omega)$ and $e^{i\left(k_z\Delta z_0-\omega\frac{\Delta z_0}{V}\right)}S_n(k_\rho,k_z,\omega)$, respectively.

The fundamental constraint linking the angular frequency ω and the longitudinal wave number k_z is derived as

$$\omega = Vk_z + b_m, \tag{1.3}$$

with m being the integer and $b_m = 2m\pi \frac{V}{\Delta z_0}$. To satisfy this constraint, the spectrum $S_n(k_\rho, k_z, \omega)$ must be of the form

$$S_n(k_\rho, k_z, \omega) = \bar{S}_n(k_z, \omega)\delta\left(k_\rho^2 - \left[\frac{\omega^2}{c^2} - k_z^2\right]\right), \tag{1.4}$$

where $\delta(\cdot)$ is the Dirac delta function. Accordingly, equation (1.2) could be written as

$$\Psi(\rho, \varphi, z, t) = \sum_{n=-\infty}^{\infty}\left[\int_0^{\infty}\int_{-\omega/c}^{\omega/c} \bar{S}_n(k_z, \omega) J_n\left(\rho\sqrt{\frac{\omega^2}{c^2} - k_z^2}\right) e^{i(k_z z - \omega t)} e^{in\varphi} dk_z d\omega\right], \tag{1.5}$$

where only the positive angular frequency components are taken into account. For non-diffracting waves, the spectrum function must conform to the constraint (1.3), thus

$$\bar{S}_n(k_z, \omega) = \sum_{m=-\infty}^{\infty} \bar{S}_{nm}(\omega)\delta(\omega - [Vk_z + b_m]), \tag{1.6}$$

with $\bar{S}_{nm}(\omega)$ being an arbitrary spectrum function.

By inserting (1.6) into (1.5), the general integral of the ideal non-diffracting wave is obtained as

$$\Psi(\rho, \varphi, z, t) = \sum_{n=-\infty}^{\infty}\sum_{n=-\infty}^{\infty} \psi_{nm}(\rho, \varphi, z, t), \tag{1.7}$$

with

$$\psi_{nm}(\rho, \varphi, z, t) = e^{-ib_m \frac{z}{V}} \int_{(\omega_{\min})_m}^{(\omega_{\max})_m} \bar{S}_{nm}(\omega) J_n\left(\rho\sqrt{\left(\frac{1}{c^2} - \frac{1}{V^2}\right)\omega^2 + \frac{2b_m}{V^2}\omega - \frac{b_m^2}{V^2}}\right) e^{i\frac{\omega}{V}(z - Vt)} e^{in\varphi} d\omega, \tag{1.8}$$

where the integration limits depend on the value of the wave's speed as follows:

- For subluminal waves $(V < c)$: $b_m > 0$, $(\omega_{\min})_m = cb_m/(c+V)$ and $(\omega_{\max})_m = cb_m/(c-V)$,

- For luminal waves $(V = c)$: $b_m > 0$, $(\omega_{\min})_m = b_m/2$ and $(\omega_{\max})_m = \infty$,
- For superluminal waves $(V > c)$: $b_m \geq 0$, $(\omega_{\min})_m = cb_m/(c+V)$ and $(\omega_{\max})_m = \infty$; or $b_m < 0$, $(\omega_{\min})_m = cb_m/(c-V)$ and $(\omega_{\max})_m = \infty$.

1.5 Generalized Bidirectional Decomposition

The method of bidirectional decomposition was first introduced by Besieris, Sharaawi and Ziolkowski [18] as a formal approach to analyze and construct different families of LW solutions. Only the axially symmetric solutions will be considered, i.e.

$$\bar{S}_n(k_z,\omega) = \delta_{n0}\bar{S}(k_z,\omega), \tag{1.9}$$

where δ_{n0} is the Kronecker delta. The wave representation in (1.5) could thus be further simplified to

$$\Psi(\rho,z,t) = \int_0^{\infty}\int_{-\omega/c}^{\omega/c} \bar{S}(k_z,\omega)J_0\left(\rho\sqrt{\frac{\omega^2}{c^2}-k_z^2}\right)e^{i(k_z z-\omega t)}dk_z d\omega. \tag{1.10}$$

Ideal non-diffracting solutions could be readily obtained from (1.10) if the spectrum function satisfies the linear relationship in (1.3). Intuitively, it is more suitable to choose new spectral parameters in place of (k_z,ω) to make the implementation easier [18]. By introducing the new spectral parameters (α,β) such that

$$\alpha = \frac{1}{2V}(\omega + Vk_z) \quad ; \quad \beta = \frac{1}{2V}(\omega - Vk_z), \tag{1.11}$$

and limiting the analysis to luminal and superluminal solutions, the wave expression in (1.10) could be written as

$$\Psi(\rho,\zeta,\eta) = \int_0^{\infty}\int_0^{\infty} S(\alpha,\beta)J_0\left(\rho\sqrt{\left(\frac{V^2}{c^2}-1\right)(\alpha^2+\beta^2)+2\left(\frac{V^2}{c^2}+1\right)\alpha\beta}\right)e^{i(\alpha\zeta-\beta\eta)}d\alpha d\beta, \tag{1.12}$$

with

$$\zeta = z - Vt \quad ; \quad \eta = z + Vt. \tag{1.13}$$

The transformation to the new representation, which also preserves the constraint (1.3), is readily implemented by letting

$$\bar{S}(k_z, \omega) \rightarrow S(\alpha, \beta) = \Phi(\alpha)\delta(\beta - \beta_0), \tag{1.14}$$

with $\beta_0 = b/2V$. The delta function $\delta(\beta - \beta_0)$ in the spectrum implies that the Bessel beams constituting the spectrum are integrated along the continuous line $\Phi(\alpha) \rightarrow \Phi(\frac{\omega}{V} - \beta_0)$, which is natural way to represent pulses with field concentration on $\rho = 0$ and $\zeta = 0$.

However, it is essential to emphasize [19] that when $\beta_0 > 0$, there exist contributions from both forward and backward traveling Bessel beams, corresponding to the frequency intervals $2V\beta_0 \leq \omega < \infty$ (where $k_z \geq 0$) and $V\beta_0 \leq \omega < V\beta_0$ (where $k_z < 0$), respectively. Physical solutions could be obtained by minimizing the contribution of the backward traveling components by choosing suitable spectrum functions.

1.6 The Focus Wave Mode Family

The bidirectional decomposition method is used to derive the traditional focus wave mode (FWM). The approach is different from that given in [1] is due to derivation of the superluminal representation of the FWM first, which is followed by the derivation of ordinary FWM. Next, a finite energy solution, termed the modified power spectrum (MPS) is derived from the FWM following [5].

1.6.1 The Ideal Non-diffracting Solution

For the spectrum function

$$S(\alpha,\beta)=aVe^{-aV\alpha}\delta(\beta-\beta_0), \tag{1.15}$$

with a a positive constant, the angular frequency spectrum of this pulse is of the type $\Phi(\alpha)\propto e^{-a\omega}$ and therefore has a $1/e$ bandwidth given by $\Delta\omega=1/a$. And as $\beta_0>0$, the spectral interval $0\le\alpha<\beta_0$ contributes only to backward traveling Bessel beams, it is necessary to have $aV\beta_0<<1$ to minimize the contribution of the backward traveling beams compared to the forward traveling ones. This condition allows for a simplification in the argument of the Bessel function in (1.12) by neglecting the term $\left(V^2/c^2-1\right)\beta_0$. This simplified expression could be written as

$$\Psi(\rho,\zeta,\eta)\approx aVe^{-i\beta_0\eta}\int_0^\infty J_0\left(\rho\sqrt{\left(\frac{V^2}{c^2}-1\right)\alpha^2+2\left(\frac{V^2}{c^2}+1\right)\alpha\beta_0}\right)e^{i\alpha(\zeta-aV)}d\alpha. \tag{1.16}$$

Using identity (6.616.1) of [20], the expression of the superluminal Focus Wave Mode (SFWM) [19] is obtained as

$$\Psi_{SFWM}(\rho,\zeta,\eta)=Xe^{-i\beta_0\eta}\exp\left(\beta_0\frac{V^2+c^2}{V^2-c^2}\left[(aV-i\zeta)-\frac{aV}{X}\right]\right), \tag{1.17}$$

with

$$X=\frac{aV}{\sqrt{(aV-i\zeta)^2+\left(\frac{V^2}{c^2}-1\right)\rho^2}}. \tag{1.18}$$

The center of the SFWM is located on $\rho=0$ and at $\zeta=0$. The intensity, $|\Psi|^2$, of the pulse propagates rigidly (no local variations); however, the complex function propagates with local variations, recovering its whole three dimensional form after each space and time intervals $\Delta z_0=\pi/\beta_0$ and $\Delta t_0=\Delta z_0/V$, respectively.

The luminal pulse is derived directly from (1.17) by letting $V\to c^+$ [19], such that

$$\Psi_{FWM}(\rho,\zeta,\eta)=ac\left(\frac{e^{-i\beta_0\eta}}{ac-i\zeta}\right)\exp\left(-\frac{\beta_0\rho^2}{ac-i\zeta}\right). \tag{1.19}$$

1.6.2 The Finite Energy Solution

A finite energy solution could be derived from the ideal solution by means of linear superposition. In particular

$$\Psi(\rho,\zeta,\eta)=\int_0^\infty \Psi_{FWM}(\rho,\zeta,\eta)F(\beta)d\beta, \tag{1.20}$$

defines a finite energy pulse if $F(\beta)/\sqrt{\beta}$ is square integrable [10].

By choosing $F(\beta)$ such that

$$F(\beta)=\begin{cases}\dfrac{(\beta-\beta_0)^{p-1}}{\Gamma(p)}e^{-q(\beta-\beta_0)}, & \beta>\beta_0\\ 0, & 0\le\beta\le\beta_0\end{cases}, \tag{1.21}$$

a finite energy solution of the form

$$\Psi_{MPS}(\rho,\zeta,\eta)=\frac{aqce^{-i\beta_0\eta}}{(ac-i\zeta)\left((q+i\eta)+\rho^2\right)^p}\exp\left(-\frac{\beta_0\rho^2}{ac-i\zeta}\right), \tag{1.22}$$

is derived [5]. This pulse is named modified power spectrum (MPS) because its spectrum is derived from the power spectrum $\beta^{p-1}e^{-q\phi}$ by scaling and truncation.

CHAPTER 2

THE TRANSVERSE ELECTRIC MODIFIED POWER SPECTRUM PULSE

2.1 Introduction

In this chapter, the TE electromagnetic counterpart of the scalar solution of (1.22) is derived using (1.22) as the magnetic Hertz potential.

The general form of the magnetic field expression is given by

$$\mathbf{H}(\mathbf{r},t)=\nabla\left(\nabla\cdot\mathbf{\Pi}^{(m)}(\mathbf{r},t)\right)+\varepsilon\nabla\times\frac{\partial}{\partial t}\mathbf{\Pi}^{(e)}(\mathbf{r},t)-\frac{1}{c^2}\mathbf{\Pi}^{(m)}(\mathbf{r},t), \tag{2.1}$$

with $\mathbf{H}(\mathbf{r},t)$ the magnetic field, ε the medium permittivity, $\mathbf{\Pi}^{(e)}(\mathbf{r},t)=0$ and $\mathbf{\Pi}^{(m)}(\mathbf{r},t)=\Psi_{MPS}(\rho,z,t)\hat{a}_z$, where $\hat{a}_\xi$ is the unit vector along the ξ-direction.

The electric field is derived from (2.1) using Maxwell's equations and is given by

$$\mathbf{E}(\rho,\zeta,\eta)=\mu\frac{\partial^2}{\partial t\partial\rho}\Psi_{MPS}(\rho,\zeta,\eta)\hat{a}_\varphi. \tag{2.2}$$

2.2 Characterization of the TE MPS Pulse

In this section, the relation between the pulse parameters and its physical properties of its electric field (2.2) is established. In what follows, and without loss of generality, the pulse parameter p will always be chosen to be equal to unity. Setting the parameter to a real value less than unity, it will slow down the decay rate of the pulse beyond the focusing range, but it will greatly enhance the backward traveling components; and if it is set to a value greater than unity, it will decrease the pulse focusing range and boost its decay [5].

2.2.1 Causality

By enforcing $\beta_0 = 0$, the resulting pulse has no backward traveling components; nevertheless, a lot of flexibility in choosing the remaining physical properties of the pulse are lost as well. Thus it is preferable to keep the parameter β_0 as a free parameter, as having $q\beta_0 >> 1$ ensures larger field depths and strong localization properties, and try to minimize the contribution of the non-causal backward traveling components.

By examining the spectrum of the MPS given by the product of (1.15) and (1.21), the ratio of the forward to backward traveling components can be approximated by

$$\frac{\bar{S}(+k_z,\omega)}{\bar{S}(-k_z,\omega)} \approx e^{-|k_z|(aV\beta_0)}. \tag{2.3}$$

Thus the conditions adopted here to minimize the non-causal components and to maintain the pulse localization are

$$ac\beta_0 << 1, \tag{2.4a}$$

$$q\beta_0 >> 1, \tag{2.4b}$$

respectively.

2.2.2 Spot Size

Due to the derivation in the ρ-direction, the field value is exactly zero at $\rho = 0$, which gives this class of pulses its name as "dark spot" pulses. The peak of the pulse ρ_0 is found by setting the first derivative with respect to ρ of the pulse expression to zero. The spot size σ is defined further by the radial distance where the field intensity value drops to the half of its maximum. These values are given by

$$\rho_0 = \sqrt{\frac{ac}{2\beta_0}}, \tag{2.5a}$$

$$\sigma = \left(1 + \frac{1}{\sqrt{2}}\right)\rho_0. \tag{2.5b}$$

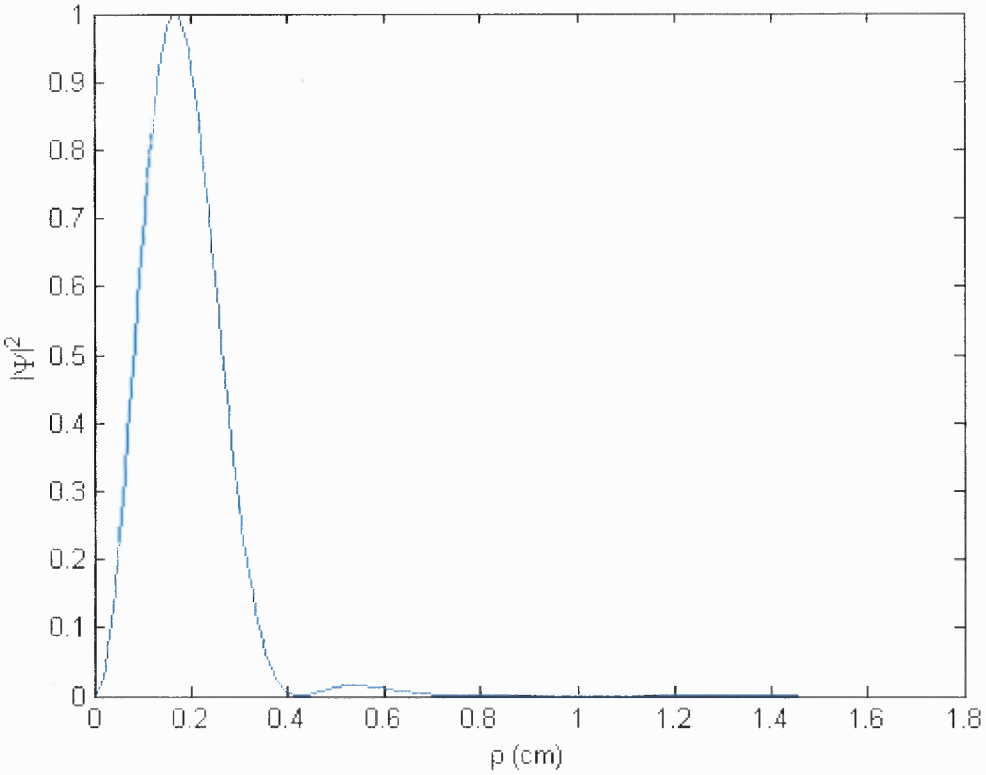

Figure 2.1 The intensity profile of a TE MPS pulse with $\beta_0 = 33.33 m^{-1}$, $a = 10^{-12}\ s$ and $q = 10^5\ m$.

Figure 2.1 shows a plot of the intensity profile of a TE MPS pulse with $\rho_0 = 0.21 cm$ and $\sigma = 0.36 cm$.

2.2.3 Bandwidth

By investigating the spectrum of the TE MPS and considering the Fourier transform property $T\left[\frac{d}{dt} f(t)\right] = i\omega T[f(t)]$, the $1/e$ bandwidth could be approximated by

$$\Delta\omega = \frac{2}{a}, \tag{2.6}$$

with the peak at

$$\omega_0 = \beta_0 c, \tag{2.7}$$

and the peak occurring at the beginning of the spectrum.

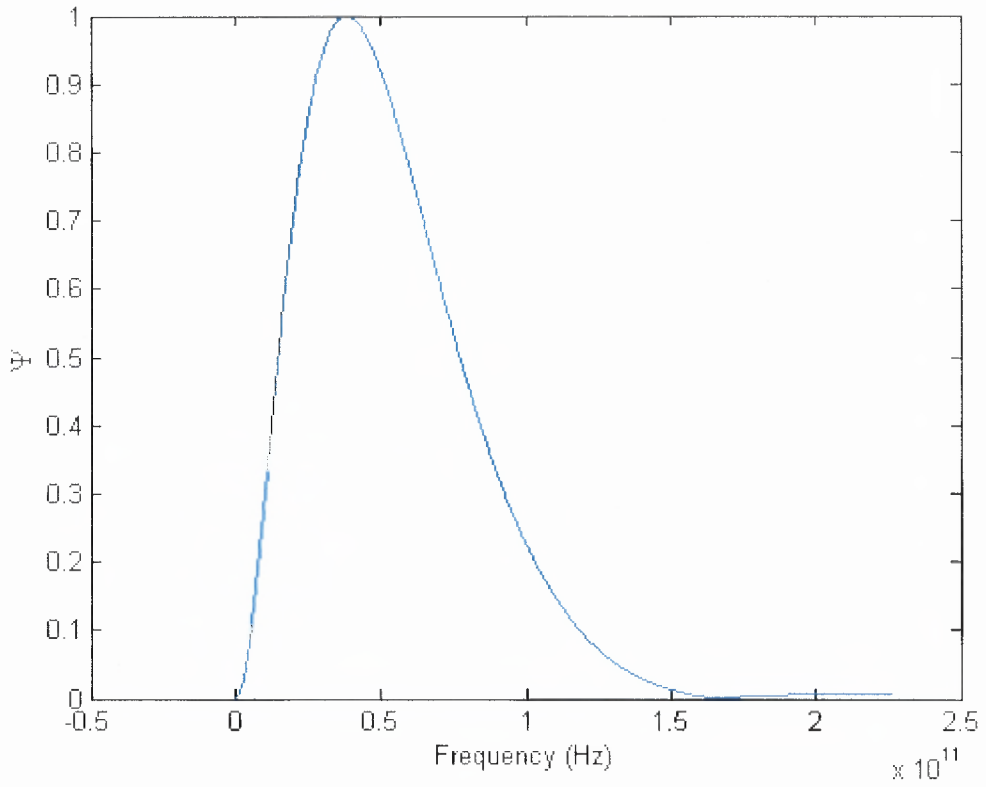

Figure 2.2 The bandwidth of a TE MPS pulse with $\beta_0 = 33.33 m^{-1}$, $a = 10^{-12}\ s$ and $q = 10^5\ m$.

Figure 2.2 shows a plot of the bandwidth of a TE MPS pulse with $\omega_0 = 10^{10}\ rad$ and $\Delta\omega = 2\times 10^{12}\ rad$.

2.2.4 Field Depth

By defining the field depth R as the distance over which the pulse's peak intensity drops to half of its initial value, then by setting $\rho = 0$ in (1.22), the depth of field is

$$R = \frac{q}{2}, \tag{2.8}$$

which solely depends on the parameter q as it regulates the concentration of the field around the line $\omega/c = k_z + 2\beta_0$.

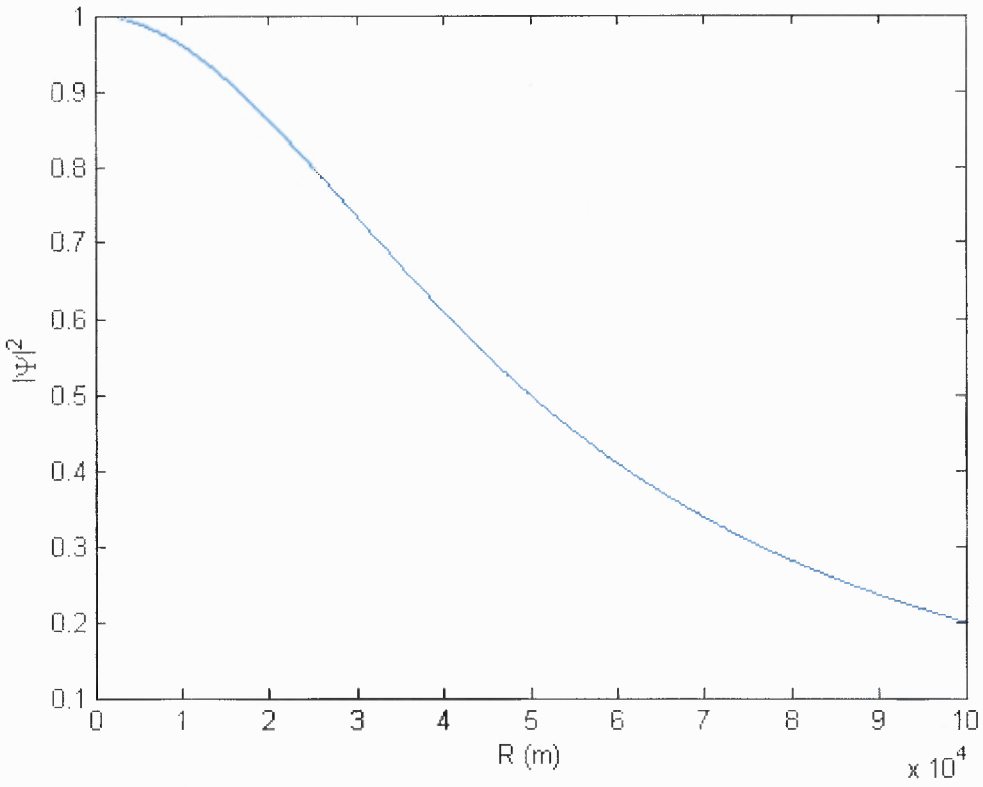

Figure 2.3 The intensity profile of a TE MPS pulse as a function of its range with $\beta_0 = 33.33\,m^{-1}$, $a = 10^{-12}\,s$ and $q = 10^5\,m$.

Figure 2.3 shows a plot of intensity profile of a TE MPS pulse as a function of propagation distance with pulse range $R = 50\,km$.

2.2.5 Longitudinal Localization

By setting $t = 0$ and $\rho = 0$ in (1.22), and defining the longitudinal extension Δz of the pulse as the length at which the pulse's intensity drops to half of its maximum, it could be shown that the longitudinal localization of the TE MPS pulse is given by

$$\Delta z = 2ac. \tag{2.9}$$

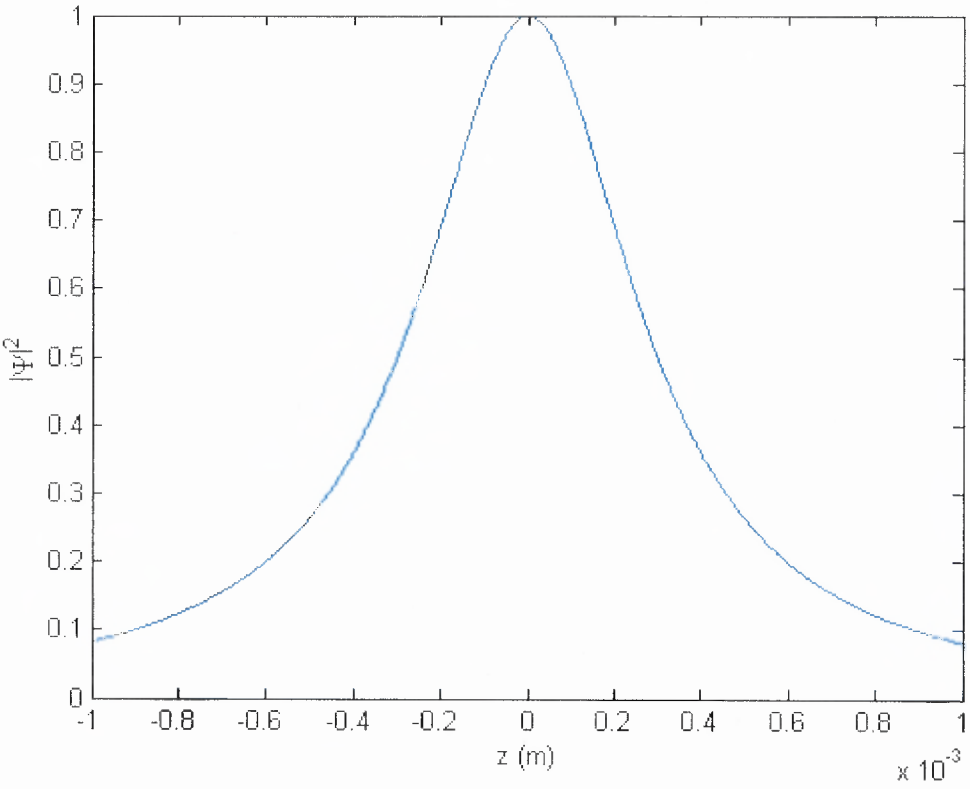

Figure 2.4 The intensity profile of a TE MPS pulse as a function of its longitudinal extension with $\beta_0 = 33.33\,m^{-1}$, $a = 10^{-12}\,s$ and $q = 10^5\,m$.

Figure 2.4 shows a plot of the longitudinal extension of a TE MPS pulse's intensity with a longitudinal localization $\Delta z = 0.6\,mm$.

CHAPTER 3

ANALYSIS

3.1 Introduction

In this chapter, the derived TE MPS pulse is decomposed in terms of a number of guided TE_{0m} modes of an air-filled metallic cylindrical waveguide. The field is matched at the open interface of the waveguide and the modes excitation coefficients are calculated. To excite the modes with the computed excitation coefficients, an excitation technique that utilizes current loops inside the waveguide is utilized.

3.2 Waveguide Modes and Orthogonality Relation

Because of the cylindrical nature of the structure, the transverse field could be derived from the longitudinal one. Given the TE nature of the pulse, only guided TE modes are considered in the analysis, and accordingly, the transverse field is derived from the longitudinal magnetic field.

The solution of Helmholtz equation for the longitudinal magnetic field component is

$$h_z = \begin{cases} CJ_n\left(k_{c,mn}\rho\right)e^{ik_{z,nm}z}e^{in\varphi}, & \rho < A \\ 0, & \rho > A \end{cases}, \tag{3.1}$$

where A designates the radius of the waveguide, C is a constant. The boundary condition is satisfied with the relation

$$\frac{\partial}{\partial\rho}J_n\left(k_{c,nm}\rho\right)\Big|_{\rho=A} = 0, \tag{3.2}$$

as the tangential electric field equals zero on the metallic wall. The roots of (3.2) are designated p'_{nm}, and the eigenvalues $k_{c,nm}$ are given by

$$k_{c,nm} = \frac{p'_{nm}}{A}. \tag{3.3}$$

By letting $n = 0$, axial symmetry is assured. The longitudinal wavenumber of the m-th mode is given by

$$k_{z,0m} = \sqrt{k_0^2 - k_{c,0m}}, \tag{3.4}$$

with k_0 the wave number in free space.

The non-zero transverse field components inside the waveguide are derived from (3.1) and are given by

$$h_\rho = -iC\frac{k_{z,0m}}{k_{c,0m}} J_1\left(k_{c,0m}\rho\right)e^{ik_{z,0m}z}, \tag{3.5a}$$

$$e_\varphi = iCZ_0\frac{k_0}{k_{c,0m}} J_1\left(k_{c,0m}\rho\right)e^{ik_{z,0m}z}. \tag{3.5b}$$

with $Z_0 = \sqrt{\mu_0/\varepsilon_0}$ the intrinsic impedance and μ_0 the permeability of free space.

The guided modes of the cylindrical metallic waveguide form a complete and bi-orthogonal set [12], with the orthogonality relation given by

$$\int_0^\infty \int_0^{2\pi} \left[\mathbf{E}_m \times \mathbf{H}_n^*\right]_z \rho d\rho d\varphi = P_n \delta_{nm}, \tag{3.6}$$

with $(\cdot)^*$ designating the complex conjugate, and the mode power P_n is

$$P_n = \frac{k_{z,n}}{2\omega\mu}\int_0^\infty \int_0^{2\pi} \left|e_{\varphi n}\right|^2 \rho d\rho d\varphi. \tag{3.7}$$

Accordingly, any axially symmetric field that is defined over the interval $[0, A]$ could be expanded in terms of a weighted summation over the TE_{0m} modes in the form

$$\Psi = \sum_n c_n e_{\varphi n}, \tag{3.8}$$

with c_n the n-th expansion coefficient. The expansion coefficients are then found using the orthogonality relation (3.6) as

$$c_n = \frac{-k_{z,n}}{2\omega\mu P_n} \int_0^{\infty} \int_0^{2\pi} \Psi h_{\rho n}^* \rho d\rho d\varphi. \tag{3.9}$$

3.3 Excitation Coefficients

The expansion coefficients of the TE MPS pulse calculated according to the modal expansion method at the plane $z = 0$ (open-ended face of the waveguide) represent the transmission coefficients as shown in Figure 3.1. It is required to determine the excitation coefficients of the guided modes. The excitation coefficients determine the needed frequency spectrum and power to excite each of the guided modes that contribute to the generation of the pulse.

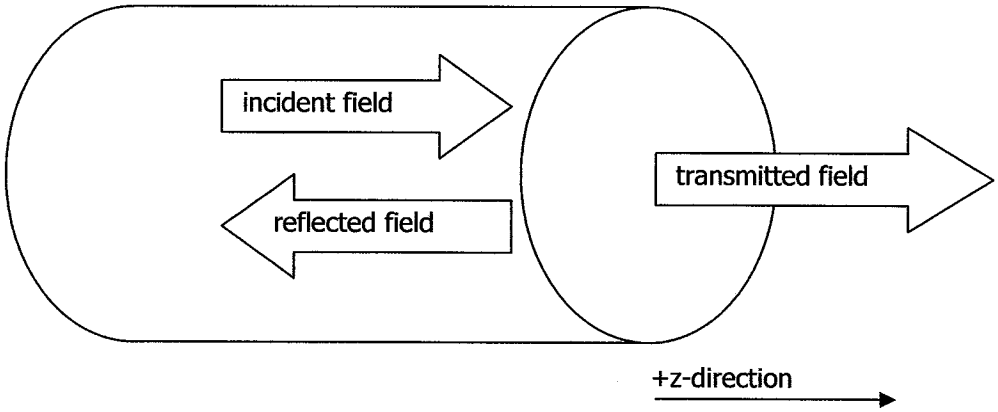

Figure 3.1 Diagram of incident, reflected and transmitted fields at the open-ended face of the waveguide.

Matching the tangential electric and magnetic fields at the interface results in

$$\sum_n [a_n + b_n] e_{\varphi n} = \sum_n c_n^{(e)} e_{\varphi n}, \tag{3.10a}$$

$$\sum_n [a_n - b_n] \frac{e_{\varphi n}}{Z_{gn}} = \sum_n c_n^{(m)} h_{\rho n}, \tag{3.10b}$$

with Z_{gn} the wave impedance of the n-th mode, a_n and b_n are the incident and reflected coefficients, respectively, and $c_n^{(e)}$ and $c_n^{(m)}$ are the transmitted electric field and magnetic field coefficients, respectively. The magnetic field expansion coefficients are obtained using the same orthogonality relation (3.9) after replacing the pulse's electric field with its magnetic field, and the mode's radial magnetic field with its azimuthal electric field. From (3.10), the needed excitation coefficients are computed using

$$a_n = \frac{1}{2}\left[c_n^{(e)} + Z_{gn} \frac{h_{\rho n}}{e_{\varphi n}} c_n^{(m)} \right]. \tag{3.11}$$

It is worth noting that the previous technique of the excitation coefficients calculations cannot be directly applied in the case of the metallic waveguide. The discontinuity of the waveguide's metallic wall introduces a discontinuity in the tangential magnetic field; hence the scattering problem needs another technique (e.g. Wiener-Hopf technique) to be solved.

Introducing a metallic flange at the open end of the waveguide forces the electric field to be zero in the radial direction at $z = 0^+$ and prevents back scattering from the edge. The numerical results of the magnetic field calculation across the discontinuity show that the using the previous technique is an acceptable approximation as the largest value of the magnetic field along the discontinuity surface is at least two orders of magnitude less than its value on the aperture. Figure 3.2 shows the proposed metallic flange extension to the waveguide.

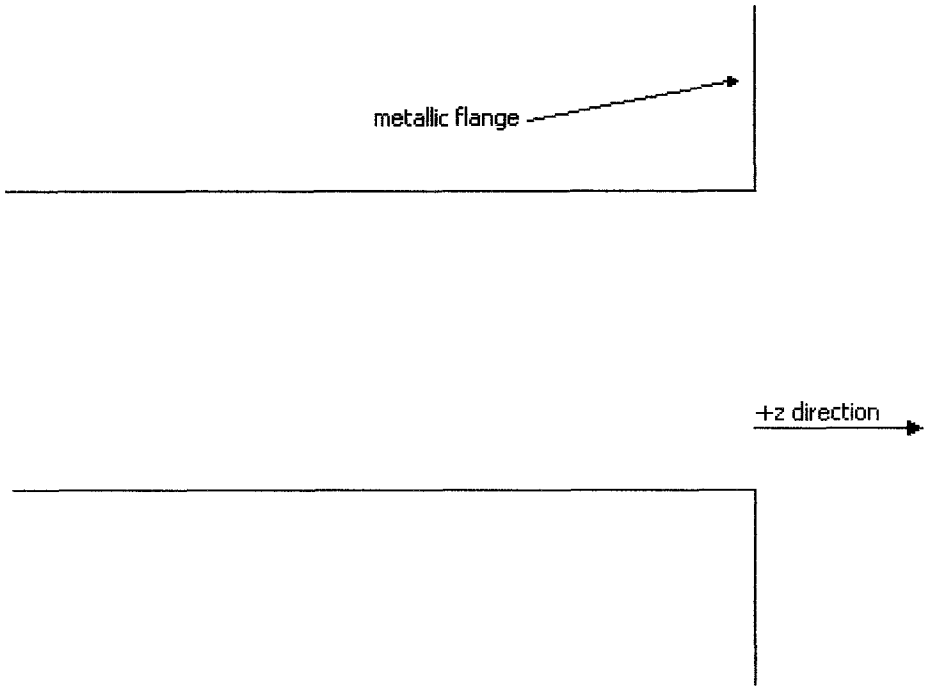

Figure 3.2 Diagram of the waveguide with a metallic flange at its open end.

3.4 Current Loops

The proposed excitation technique uses circular current loops having different radii ρ_m and positioned at different locations with respect to the open end of the waveguide z_m. It is required to find the temporal excitation function, which represents the time variation of the current passing through each of the circular loops.

Starting from the inhomogeneous Helmholtz equation for the longitudinal magnetic field $h_z(\mathbf{r},t)$, to excite axially symmetric TE modes,

$$(\nabla^2 + k^2)h_z(\rho,z,\omega) = -\sum_m F_m(\omega)\frac{\delta(z-z_m)\delta(\rho-\rho_m)}{\rho}, \tag{3.12}$$

where ∇^2 is the Laplacian and $F_m(\omega)$ is the frequency spectrum of the excitation current of the m-th loop.

The longitudinal magnetic field is expanded in terms of the complete orthonormal set

$$e_{\varphi n} = N_n J_0(k_{c,n}\rho), \tag{3.13}$$

with the normalization coefficient $N_n = \sqrt{2}/(AJ_0(k_{c,n}A))$. Substituting into (3.12) for each loop yields

$$(\nabla^2 + k^2)\sum_n g_n(z) N_n J_0(k_{c,n}\rho) = -F_m(\omega)\frac{\delta(z-z_m)\delta(\rho-\rho_m)}{\rho}, \tag{3.14}$$

and applying the orthogonality relation of the modes (3.6)

$$\left[\frac{d^2}{dz^2} + k_{z,n}^2\right] g_n(z) = -F_m(\omega) J_0(k_{c,n}\rho_m)\delta(z-z_m). \tag{3.15}$$

The solution of (3.15) is given by

$$g_n(z) = \begin{cases} A_n(\omega)e^{ik_{z,n}z}, & z > z_m \\ B_n(\omega)e^{-ik_{z,n}z}, & z < z_m \end{cases}. \tag{3.16}$$

Applying the source conditions,

$$A_n(\omega)e^{ik_{z,n}z_m} = B_n(\omega)e^{-ik_{z,n}z_m}, \tag{3.17a}$$

$$ik_{z,n}\left(A_n(\omega)e^{ik_{z,n}z_m} + B_n(\omega)e^{-ik_{z,n}z_m}\right) = -F(\omega)J_0(k_{c,n}\rho_m), \tag{3.17b}$$

which imply the continuity of $g_n(z)$ at $z = z_m$ and the discontinuity of its derivative with respect to z at the same location. Solving for the forward traveling modes coefficients yield

$$A_n(\omega) = \frac{i}{2k_{z,n}}\left[F_m(\omega)J_0(k_{c,n}\rho_m)e^{-ik_{z,n}z_m}\right], \tag{3.18}$$

thus for $z > \max(z_m)$

$$h_z(\rho,z,\omega) = \sum_n\sum_m \frac{iN_n}{2k_{z,n}}\left[F_m(\omega)J_0(k_{c,n}\rho_m)e^{-ik_{z,n}z_m}\right]J_0(k_{c,n}\rho)e^{ik_{z,n}z}. \tag{3.19}$$

The azimuthal electric field is derived from (3.19) using Maxwell's equations, and accordingly its excitation coefficients, $C_n(\omega)$, are given by

$$C_n(\omega) = \frac{N_n}{2k_{z,n}} \sum_m F_m(\omega) J_0(k_{c,n}\rho_m) e^{-ik_{z,n}z_m}. \tag{3.20}$$

By restricting the number of current loops, m, to the number of TE modes, n, a linear system of equations could be obtained and inverted to get the current excitation spectrum as

$$\mathbf{F} = \mathbf{L}^{-1}\mathbf{C}, \tag{3.21}$$

with the matrix elements

$$L_{nm} = \frac{N_n}{2k_{c,n}} J_0(k_{c,n}\rho_m) e^{-ik_{z,n}z_m}. \tag{3.22}$$

To account for the multiple reflections from the closed end of the waveguide, all elements of (3.22) must be multiplied by $1 - e^{2ik_{z,n}|z_g - z_m|} / 1 + R_n e^{2ik_{z,n}z_g}$, with z_g the length of the waveguide section and R_n the n-th mode reflection coefficient from the waveguide's open end.

CHAPTER 4

NUMERICAL EXAMPLES

4.1 Introduction

To demonstrate the feasibility of the suggested method, two numerical examples are given. Two different pulses are used, where first the TE MPS is designed and decomposed in terms of the waveguide's modes, then the excitation coefficients are calculated as well as the currents needed to excite them. The current loops are placed inside the waveguide in two different configurations for each pulse. The efficiency of the generation process is evaluated and the accuracy of the generated pulse is examined. Interactions between adjacent current loops are omitted. Finally, numerical error analysis is performed to give a feel of the sensitivity of the suggested method. All numerical analysis is done on MATLAB™ and the code could be directly obtained by contacting the author.

4.2 Example 1

For comparison purposes, the generated pulse is designed to have the same parameters as the pulse reported in [19]. The pulse parameters are $\beta_0 = 33.33 m^{-1}$, $a = 10^{-12} s$ and $q = 10^5 m$. The parameters translate to the physical properties of a peak center at $\rho_0 = 0.21 cm$ with a spot size of $\sigma = 0.36 cm$, frequency center at $\omega_0 = 10^{10} rad$ with a $1/e$ bandwidth of $\Delta\omega = 2 \times 10^{12} rad$, a field depth $R = 50 km$ and a longitudinal localization of $\Delta z = 0.6 mm$, as shown in Figures 2.1 to 2.4, respectively. Figures 4.1 and 4.2 show the spot size and the intensity plot of the pulse, respectively.

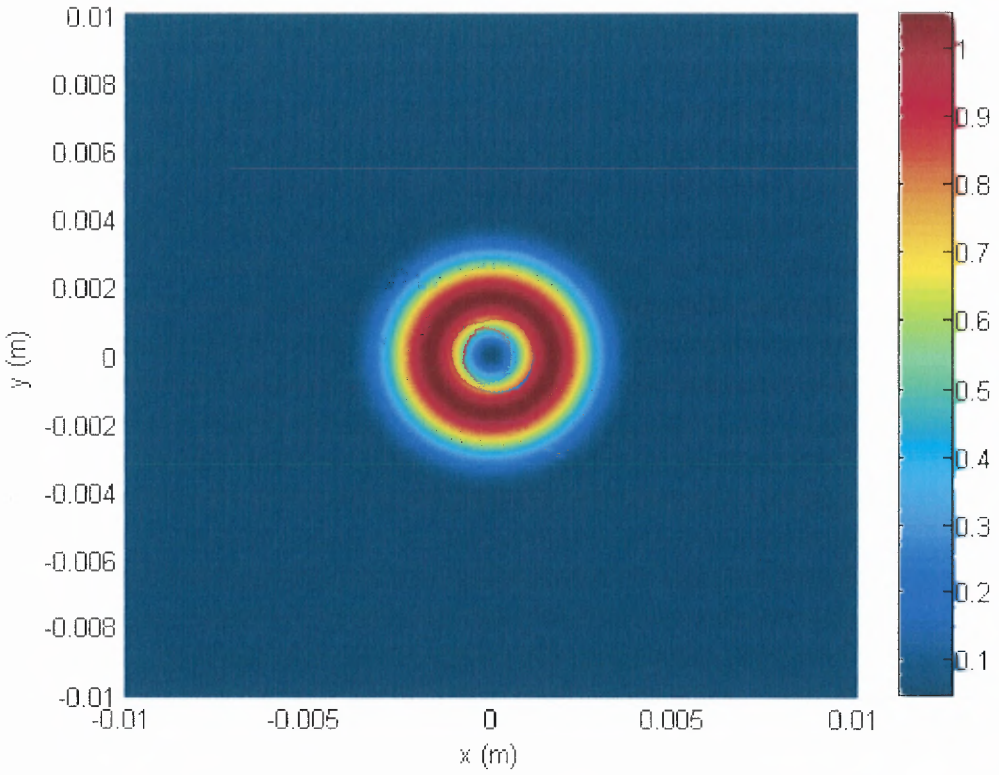

Figure 4.1 Spot intensity plot of the TE MPS pulse with $\beta_0 = 33.33\,m^{-1}$, $a = 10^{-12}\,s$ and $q = 10^5\,m$.

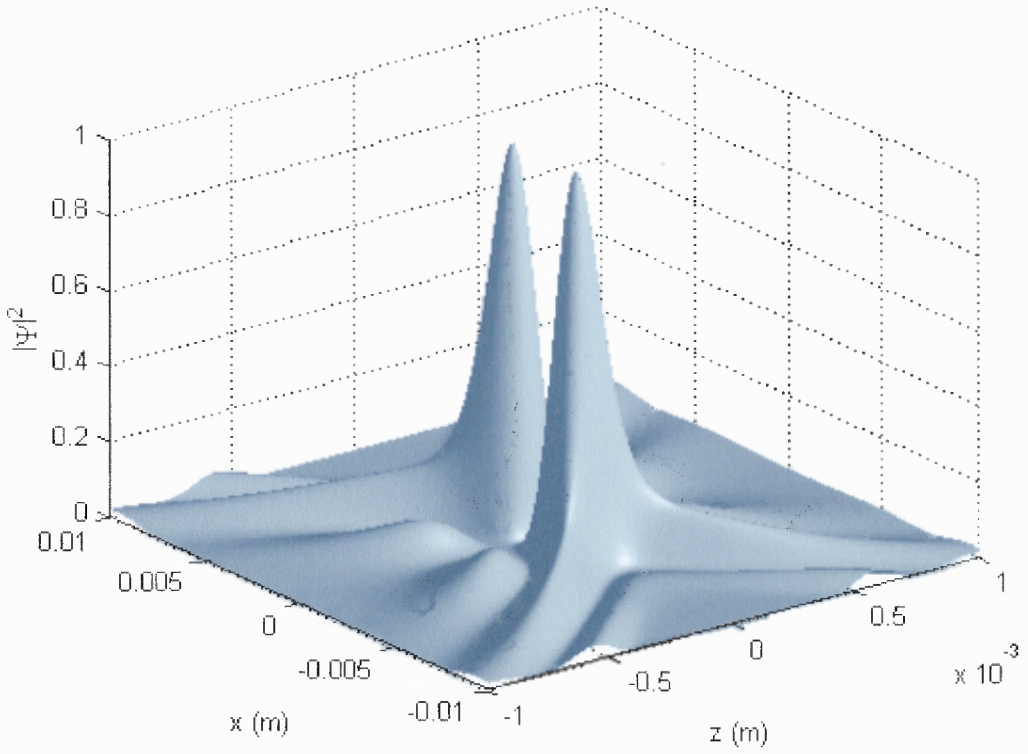

Figure 4.2 Intensity plot of the TE MPS pulse with $\beta_0 = 33.33 m^{-1}$, $a = 10^{-12}\ s$ and $q = 10^5\ m$.

4.2.1 Modal Decomposition

To estimate the appropriate number of modes in decomposition of the pulse, an initial decomposition over the first 32 TE_{0m} modes of a cylindrical waveguide with radius $A = 35.71 \times 10^{-3}\ m$ is performed. Figure 4.3 shows the power contribution of each of the modes to the total pulse power. As shown in the figure, the main power is concentrated in eight consecutive modes starting at TE_{09}.

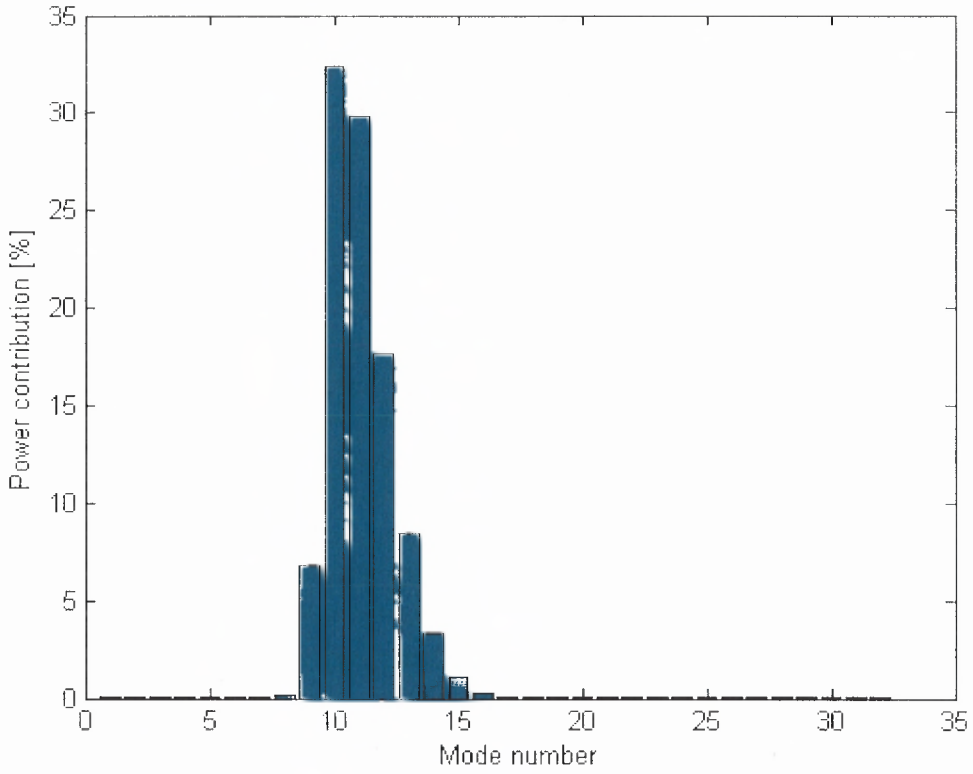

Figure 4.3 Power percentage contribution of the first 32 TE_{0m} modes for the pulse in Example 1.

The excitation coefficients are computed from the pulse expansion coefficients at the waveguide's open end as described in section 4.3.3. The resulting modes excitation coefficients are shown in Figure 4.4.

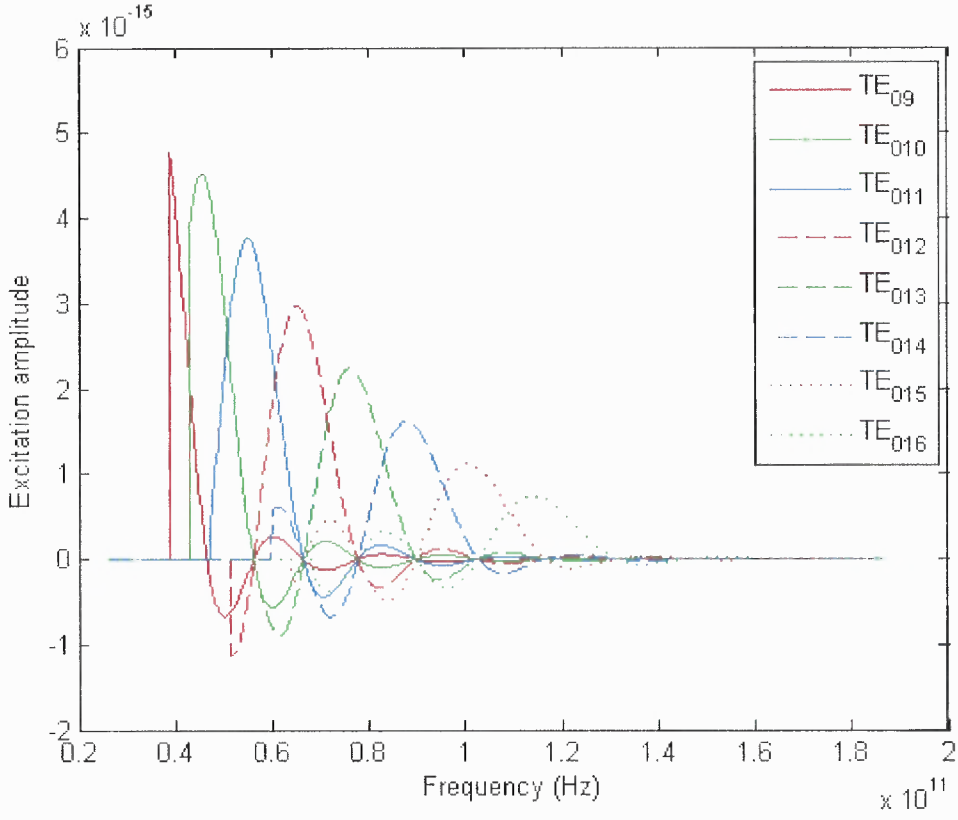

Figure 4.4 Modes Excitation coefficients of the first 8 modes starting at TE_{09} for the pulse in Example 1.

4.2.2 Excitation Configuration 1

For the first excitation configuration, eight current loops with increasing radii of $2.5\,mm$ steps and equal separation steps of $5\,mm$ from each other are used. The radii and locations are given in Table 4.1. The open end of the waveguide is located at $z = 0$.

Table 4.1 List of current loops radii and location for the first excitation method for Example 1 pulse.

Loop number	Radius (m)	Location (m)
1	0.0075	-0.080
2	0.0100	-0.085
3	0.0125	-0.090
4	0.0150	-0.095
5	0.0175	-0.100
6	0.0200	-0.105
7	0.0225	-0.110
8	0.0250	-0.115

The corresponding currents as functions of time are shown in Figure 4.5, and their corresponding spectra are shown in Figure 4.6.

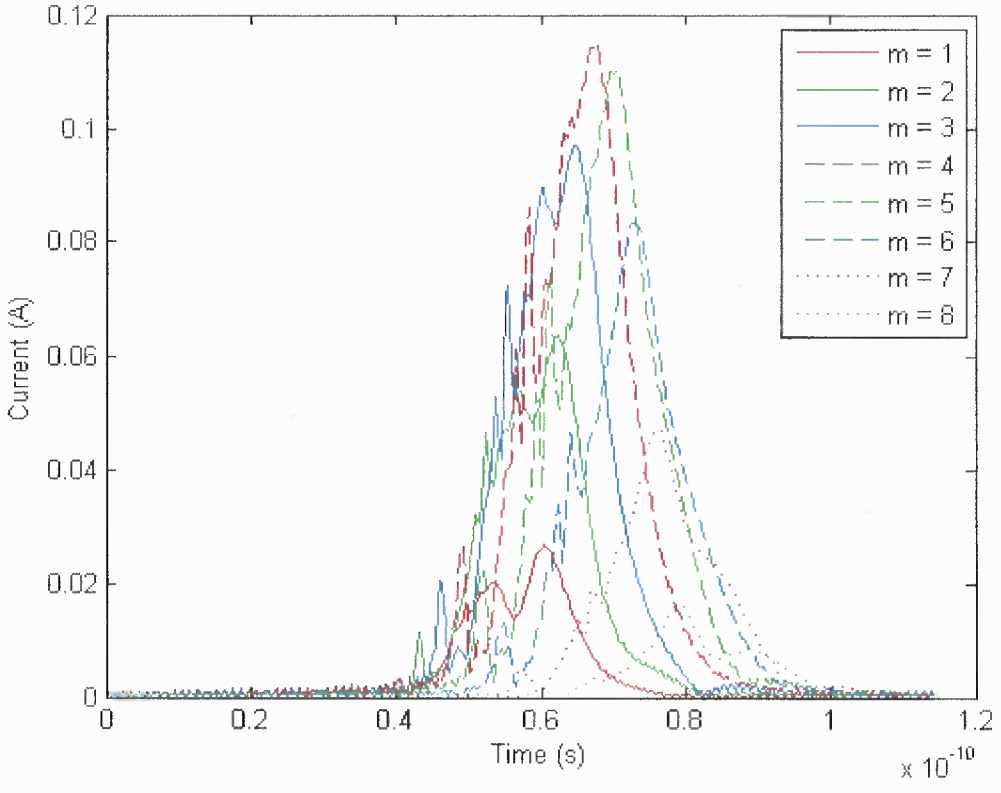

Figure 4.5 Excitation currents of configuration 1 for the pulse in Example 1.

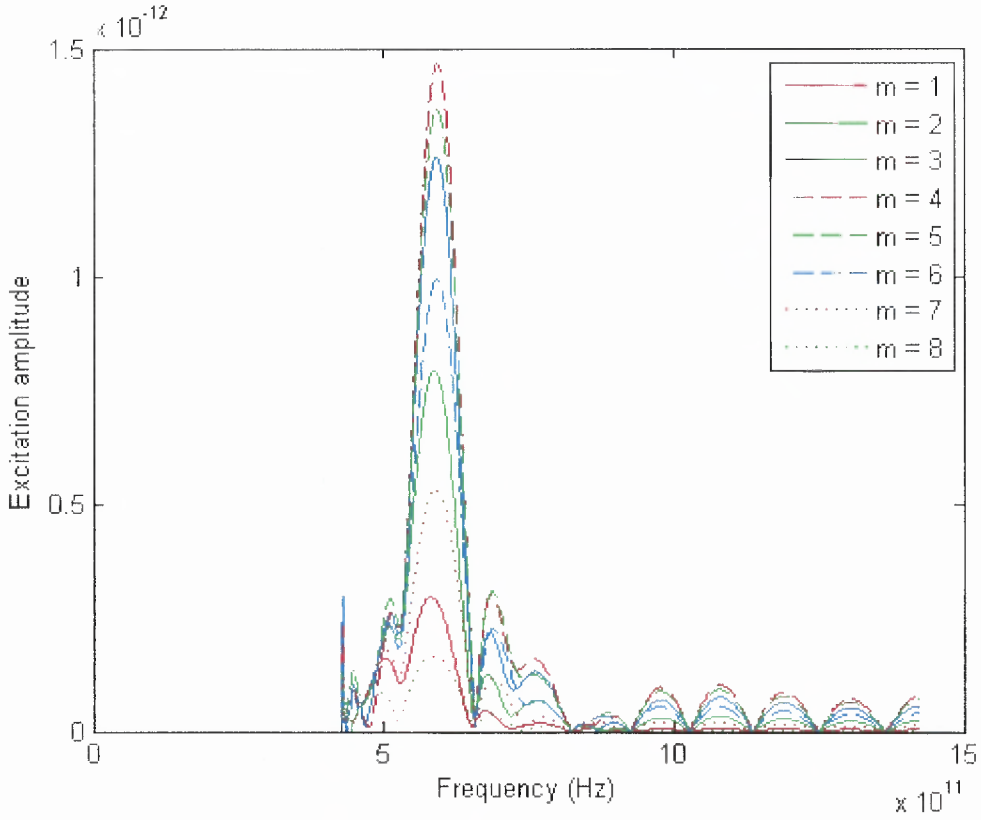

Figure 4.6 Spectra of the excitation currents of Configuration 1 for the pulse in Example 1.

The TE MPS pulse is reconstructed from the computed currents by means of solving the forward excitation problem. Figure 4.7 shows a comparison between the original and the reconstructed pulse's intensity profiles at the open end of the waveguide.

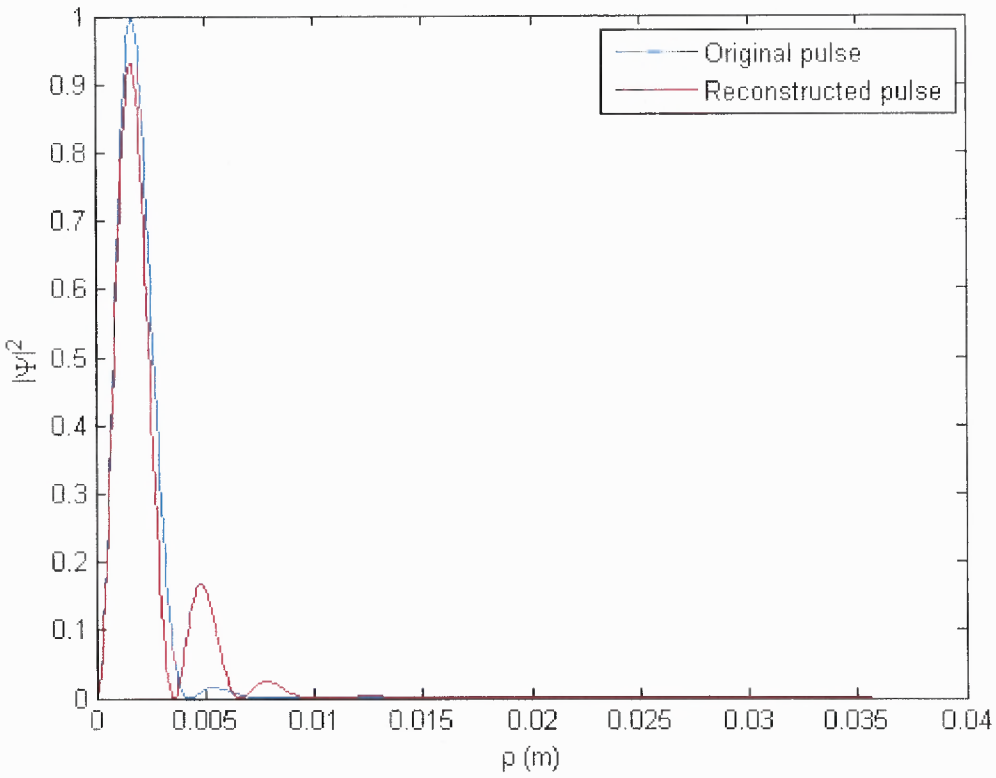

Figure 4.7 Comparison of the intensity profiles of the original and reconstructed pulses for Configuration 1 in the Example 1.

Figure 4.7 shows that the transverse localization of the pulse is preserved, although the reconstructed pulse suffers from a small decrease in intensity as well as higher power concentration in the outer ring.

To demonstrate the time localization of the reconstructed pulse, the time profiles of both the original and the reconstructed pulses are compared in Figure 4.8.

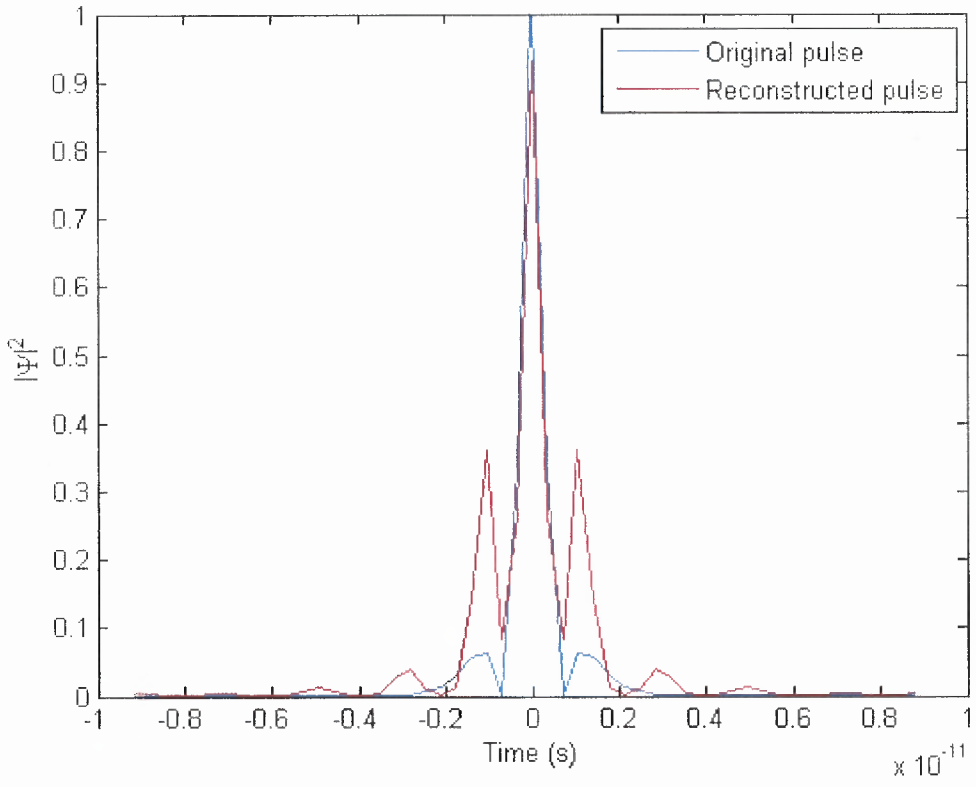

Figure 4.8 Comparison of the time profile of the intensities of the original and reconstructed pulses for Configuration 1 in the Example 1.

4.2.3 Excitation Configuration 2

The second excitation configuration uses the same loop radii as Configuration 1, but the separation between the loops is decreased to $3.33mm$. Table 2 lists the radii and locations of the current loops for Configuration 2.

Table 4.2 List of current loops radii and location for the second excitation method pulse in the Example 1.

Loop number	Radius (m)	Location (m)
1	0.0075	-0.020
2	0.0100	-0.023
3	0.0125	-0.027
4	0.0150	-0.030
5	0.0175	-0.033
6	0.0200	-0.037
7	0.0225	-0.040
8	0.0250	-0.043

The corresponding currents as functions of time are shown in Figure 4.9, and their corresponding spectra are shown in Figure 4.10.

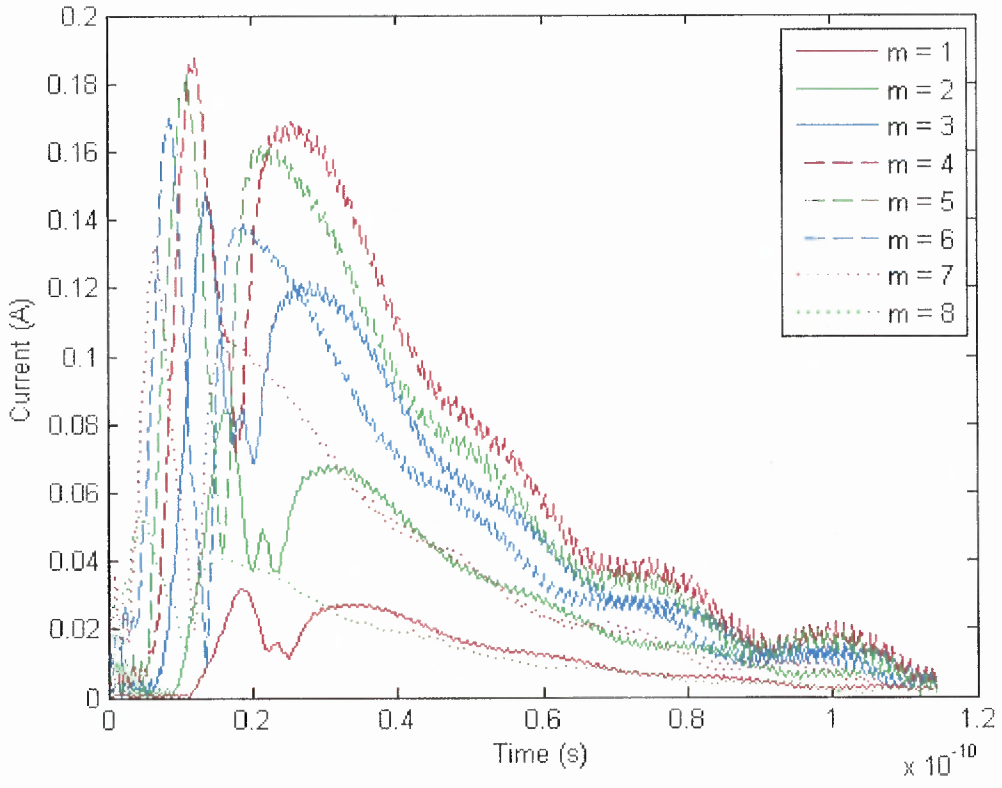

Figure 4.9 Excitation currents of configuration 2 pulse in the Example 1.

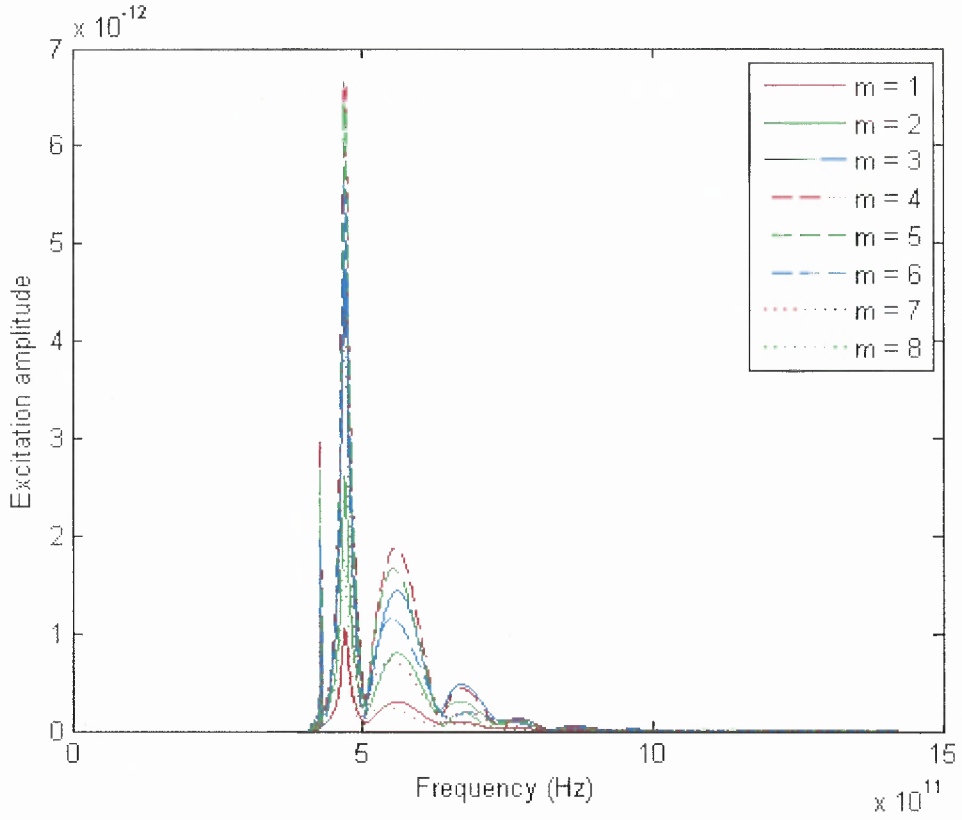

Figure 4.10 Spectra of the excitation currents of Configuration 2 pulse in Example 1.

By solving the forward problem, the field of the reconstructed pulse is computed. Figure 4.11 shows the intensity profile comparison between the original and reconstructed pulse at the open end of the waveguide. The time profile of the intensities of both the original and reconstructed pulses is depicted in Figure 4.12.

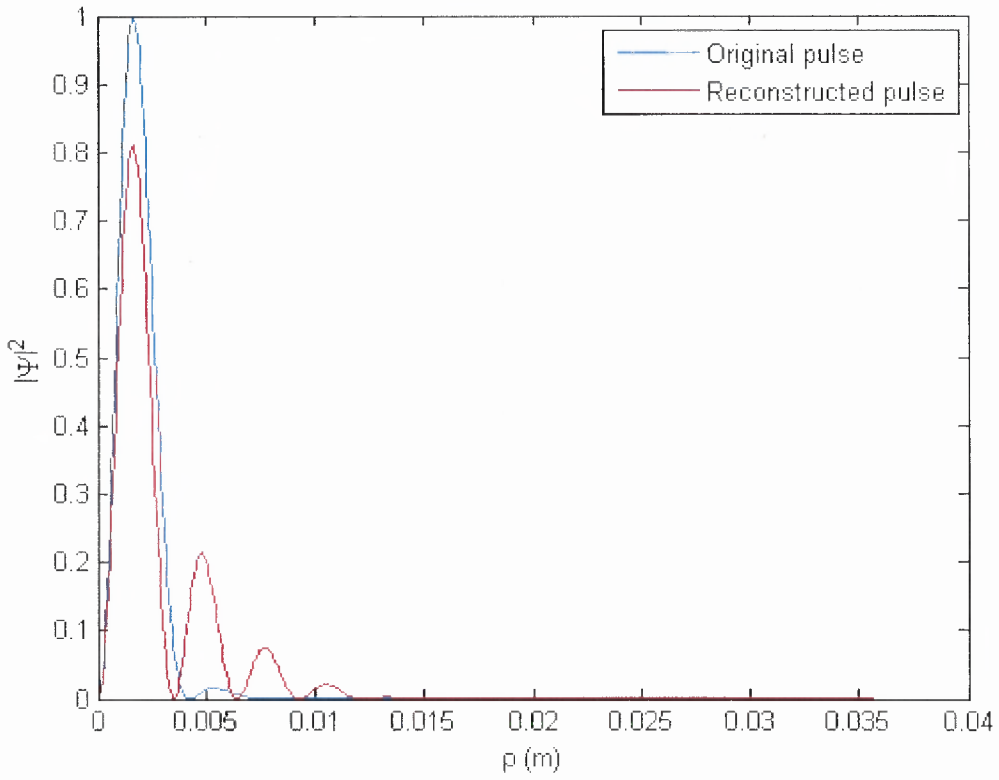

Figure 4.11 Comparison of the intensity profiles of the original and reconstructed pulses for Configuration 2 in the Example 1.

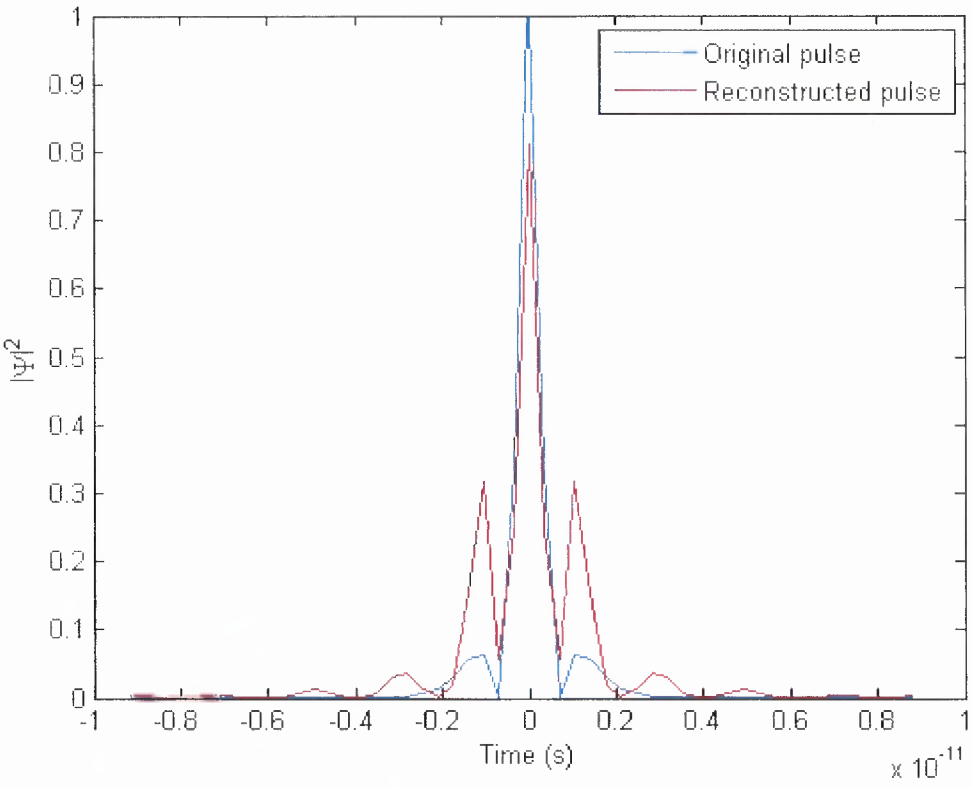

Figure 4.12 Comparison of the time profile of the intensities of the original and reconstructed pulses for Configuration 2 in the Example 1.

Figures 4.11 and 4.12 show that still both the transverse variation and localization are preserved, while the level of ripples in the profile has increased and the peak value has decreased.

4.2.4 Accuracy and Efficiency

An exact pulse generation is only possible if the number modes used is infinite. However, using an infinite number of guided modes to represent the pulse's spectrum is not possible for practical considerations. Due to these limitations, it was necessary to calculate the accuracy of the generation process. The accuracy is calculated by means of the root mean square (rms) error between the original pulse and the reconstructed one at the aperture (open end of the waveguide). The original pulse field values were calculated

at the same grid points as the reconstructed one and the rms error percentage is calculated according to:

$$\Delta_{rms} = \sqrt{\frac{1}{n}\sum_{n}\left(E_{en} - E_{rn}\right)^2}, \tag{4.1}$$

where E_{en} is the original pulse field and E_{rn} is the generated field, both evaluated at the same gird points n.

The efficiency of the pulse generation is evaluated in terms of the output-to-input powers ratio. The power losses occur because of the different wave impedances between the waveguide and the pulse propagation region (free space). The difference in impedances results in reflections at the discontinuity surface between the guiding structure and the free space. Assuming no losses in the metallic waveguide, the power efficiency is calculated in terms of the ratio of the squares of the transmitted field to the field constructed from the excitation coefficients, as

$$\gamma = \frac{1}{n}\sum_{n}\frac{\sum_{m}\left|C_m e_{\varphi n}\right|^2}{\sum_{m}\left|A_m e_{\varphi n}\right|^2}, \tag{4.2}$$

where n designates the number of sampling points and m the number of modes in which the pulse is decomposed into.

The accuracy and efficiency of the two excitation configurations are listed in Table 4.3.

Table 4.3 Accuracy and efficiency of the excitation configurations for example pulse 1.

Configuration	**Accuracy (Δ_{rms})**	**Efficiency (γ)**
1	5.72%	97.7%
2	13.5%	98.0%

Table 4.3 shows that Configuration 1 produces pulses with slightly better accuracy. The power efficiency of both methods is almost equal. The high efficiency is mainly due to the introduction of the metallic flange at the open end of the waveguide, which prevents diffraction from the edge, and also due to the strong causality nature of the pulse.

4.3 Example 2

For the second example, a more physically realizable pulse is considered. Starting with the physical requirements to have a pulse in the microwave X-band with a bandwidth not exceeding $4\,GHz$, the following pulse parameters are used $\beta_0 = 210\,m^{-1}$, $a = 4.5\times10^{-10}\,s$ and $q = 4\,m$. The resulting pulse has its peak center at $\rho_0 = 1.79\,cm$ with a spot size of $\sigma = 3.06\,cm$, frequency center at $\omega_0 = 2\pi\times10^{10}\,rad$ with a $1/e$ bandwidth of $\Delta\omega = 4.45\times10^{9}\,rad$, a field depth $R = 2\,m$ and a longitudinal localization of $\Delta z = 27.0\,cm$. Figures 4.13 to 4.16 show the physical properties of the pulse, while Figures 4.17 and 4.18 show the spot size and the intensity plot of the pulse, respectively.

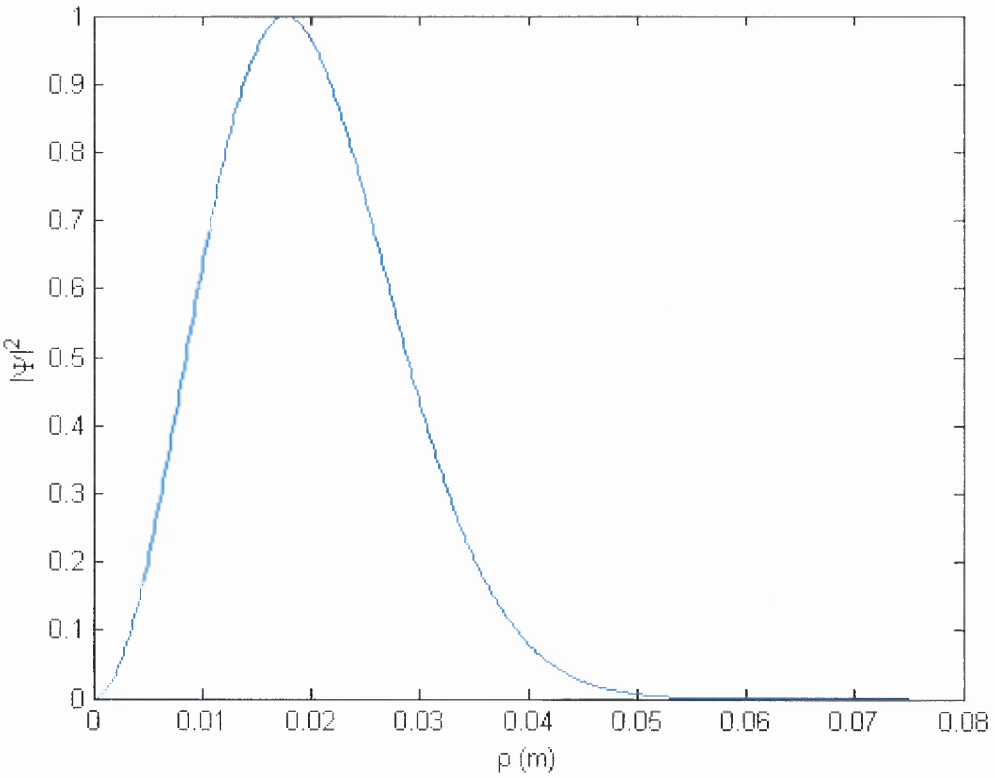

Figure 4.13 The intensity profile of a TE MPS pulse with $\beta_0 = 210\,m^{-1}$, $a = 4.5\times10^{-10}\,s$ and $q = 4\,m$.

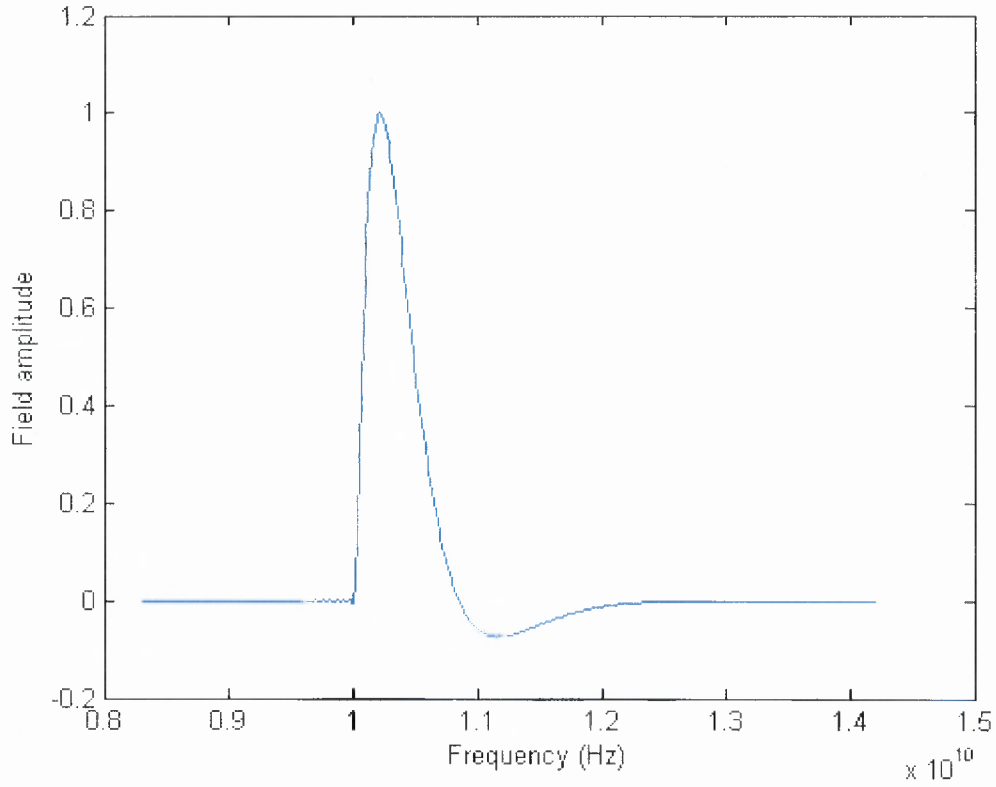

Figure 4.14 The bandwidth of a TE MPS pulse with $\beta_0 = 210\,m^{-1}$, $a = 4.5\times10^{-10}\,s$ and $q = 4\,m$.

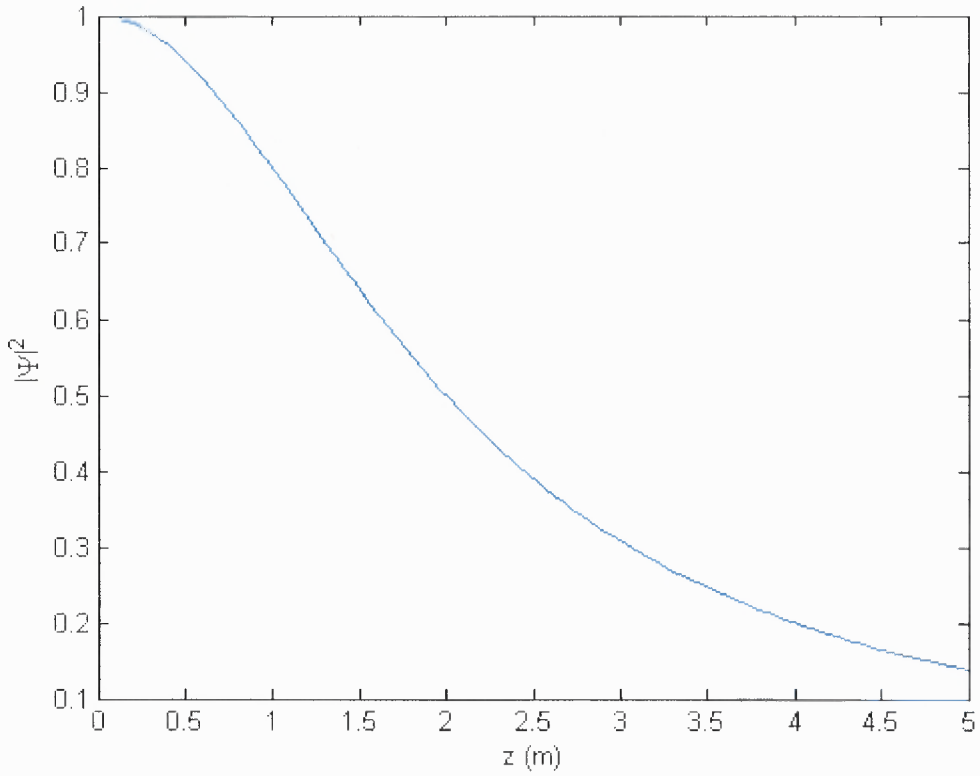

Figure 4.15 The intensity profile of a TE MPS pulse as a function of its range with $\beta_0 = 210\,m^{-1}$, $a = 4.5\times10^{-10}\,s$ and $q = 4\,m$.

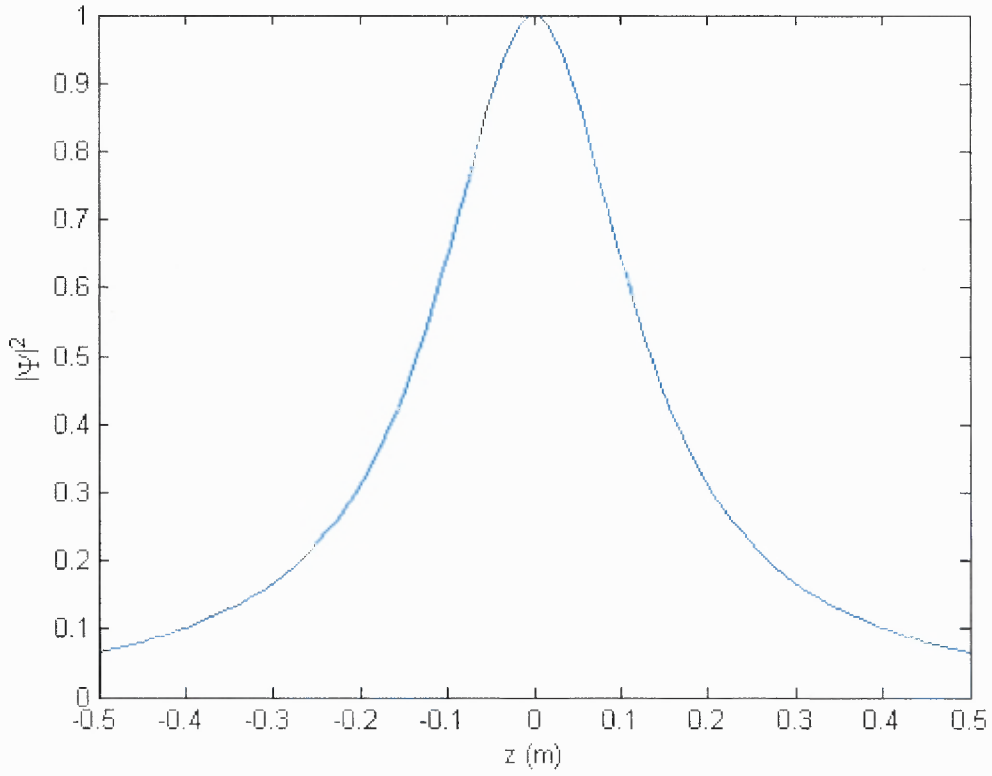

Figure 4.16 The intensity profile of a TE MPS pulse as a function of its longitudinal extension with $\beta_0 = 210\,m^{-1}$, $a = 4.5\times10^{-10}\,s$ and $q = 4\,m$.

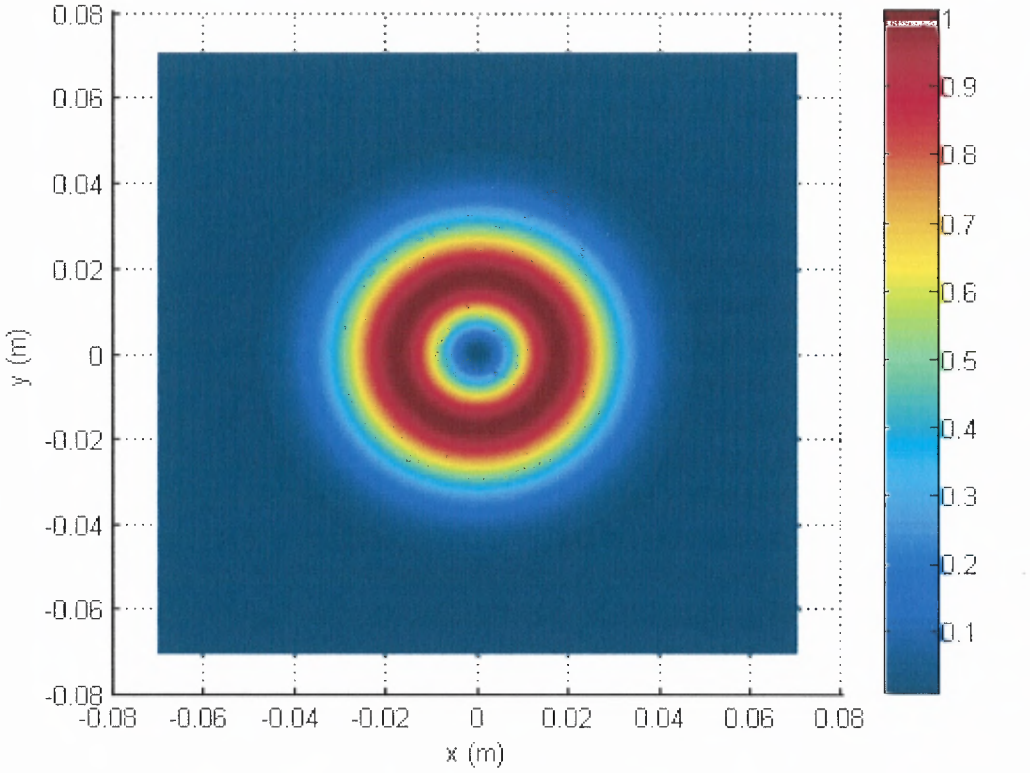

Figure 4.17 Spot intensity plot of the TE MPS pulse with $\beta_0 = 210\,m^{-1}$, $a = 4.5\times10^{-10}\,s$ and $q = 4\,m$.

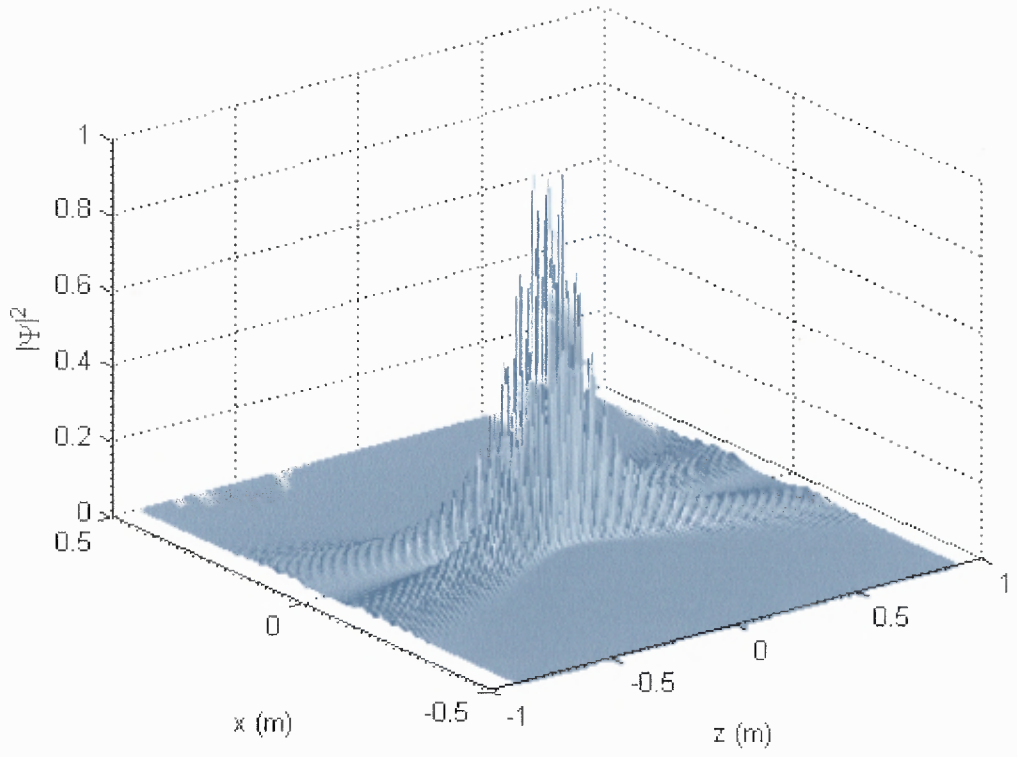

Figure 4.18 Intensity plot of the TE MPS pulse with $\beta_0 = 210\,m^{-1}$, $a = 4.5\times10^{-10}\,s$ and $q = 4\,m$.

4.3.1 Modal Decomposition

As previously done, to estimate the appropriate number of modes to decompose the pulse into, an initial decomposition over the first 32 TE_{0m} modes of a cylindrical waveguide with radius $A = 15\,cm$ is performed. Figure 4.19 shows the power contribution of each of the modes to the total pulse power. As shown in the figure, the main power is concentrated in the first six modes. Accordingly, in the first excitation configuration, all six modes will be included, while for the second configuration, only first four modes will be considered.

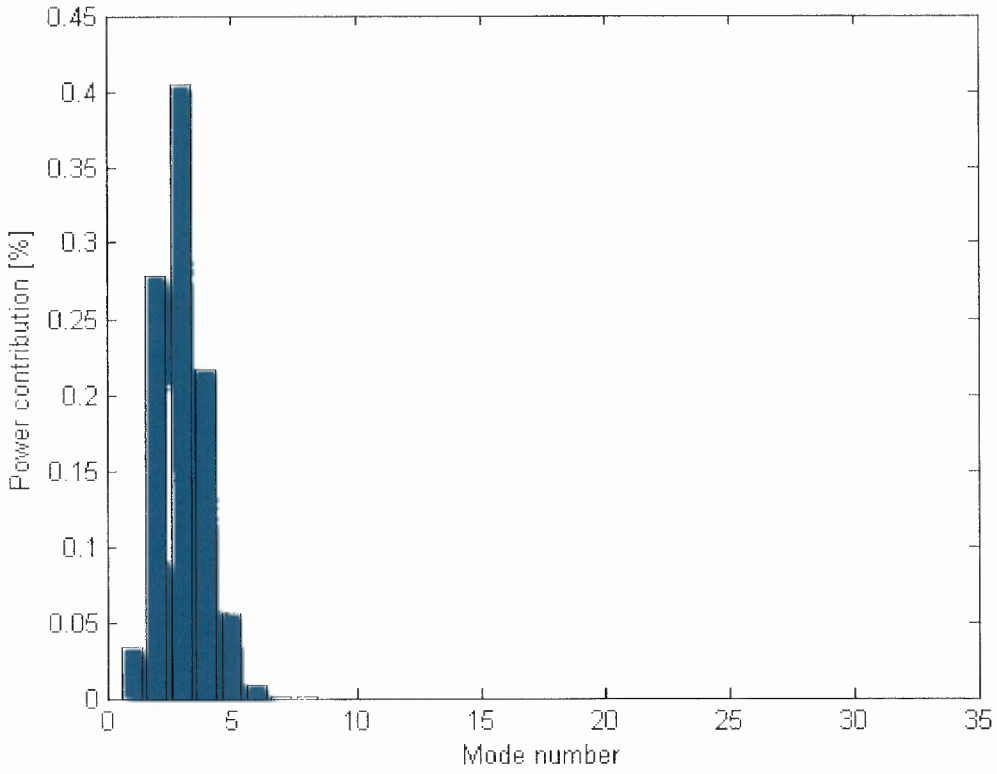

Figure 4.19 Power percentage contribution of the first 32 TE_{0m} modes for example 2 pulse.

The excitation coefficients are computed from the pulse expansion coefficients at the waveguide's open end as described in section 4.3.3. The resulting modes excitation coefficients are shown in Figure 4.20.

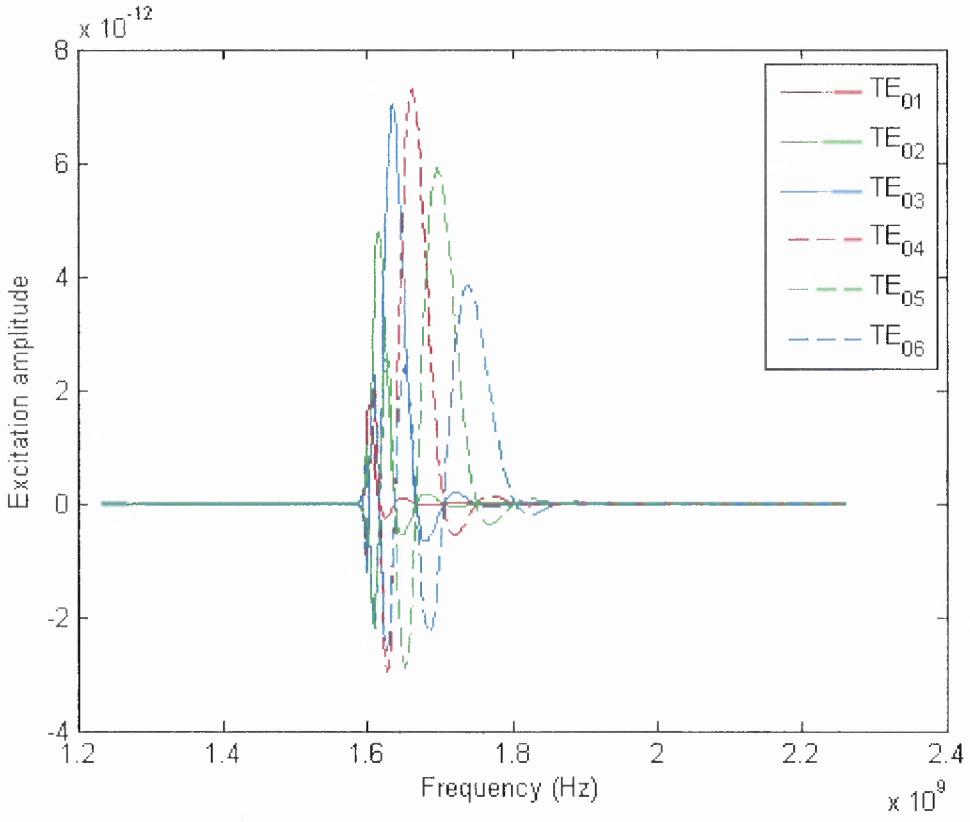

Figure 4.20 Modes Excitation coefficients of the first 6 modes for example 2 pulse.

4.3.2 Excitation Configuration 1

For the first excitation configuration, six current loops with increasing radii of $2\,cm$ steps and equal separation steps of $1\,mm$ from each other are used. The radii and locations are given in Table 4.4.

Table 4.4 List of current loops radii and locations for the excitation of the pulse in the Example 2.

Loop number	Radius (m)	Location (m)
1	0.10	-0.050
2	0.08	-0.051
3	0.06	-0.052
4	0.04	-0.053
5	0.02	-0.053
6	0.01	-0.055

The corresponding currents as functions of time are shown in Figure 4.21, and their corresponding spectra are shown in Figure 4.22.

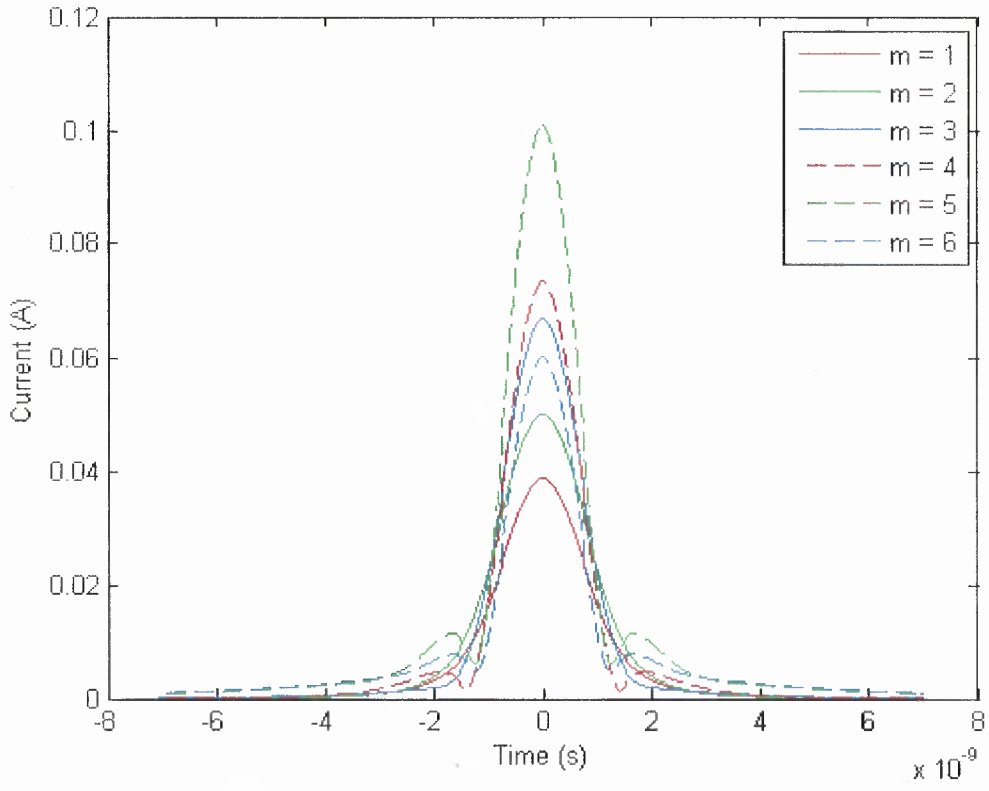

Figure 4.21 Excitation currents of configuration 1 pulse in the Example 2.

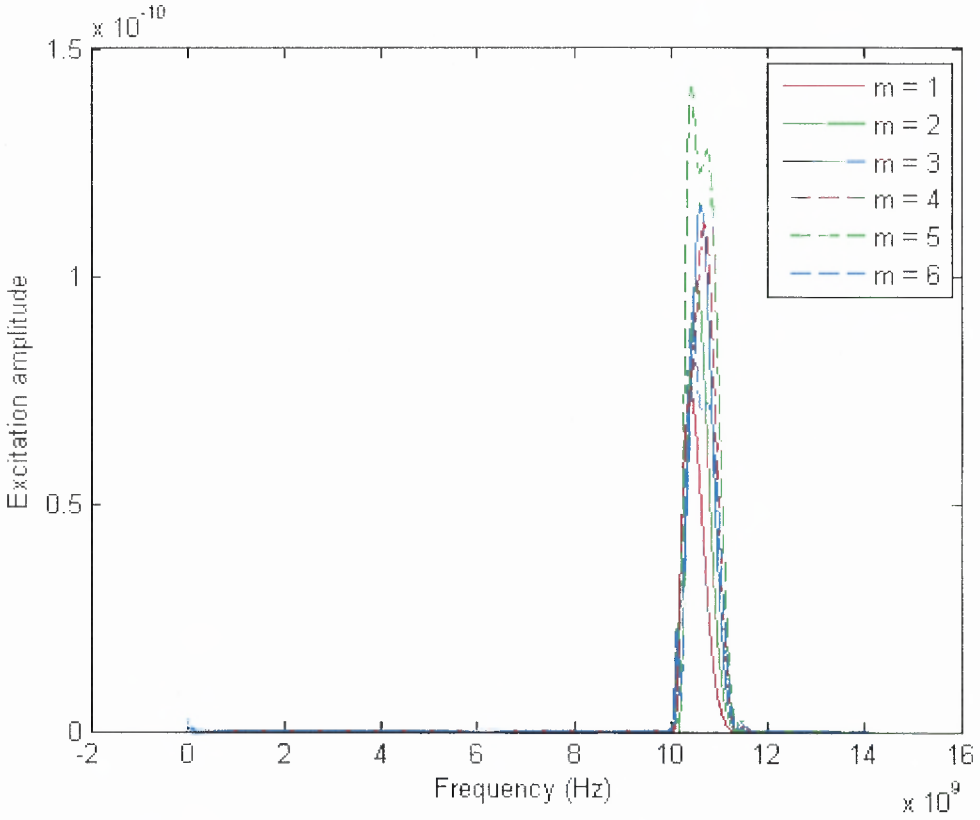

Figure 4.22 Spectra of the excitation currents of configuration 1 pulse in the Example 2.

The TE MPS pulse is reconstructed from the computed currents by means of solving the forward excitation problem. Figure 4.23 shows a comparison between the original and the reconstructed pulse's intensity profiles at the open end of the waveguide.

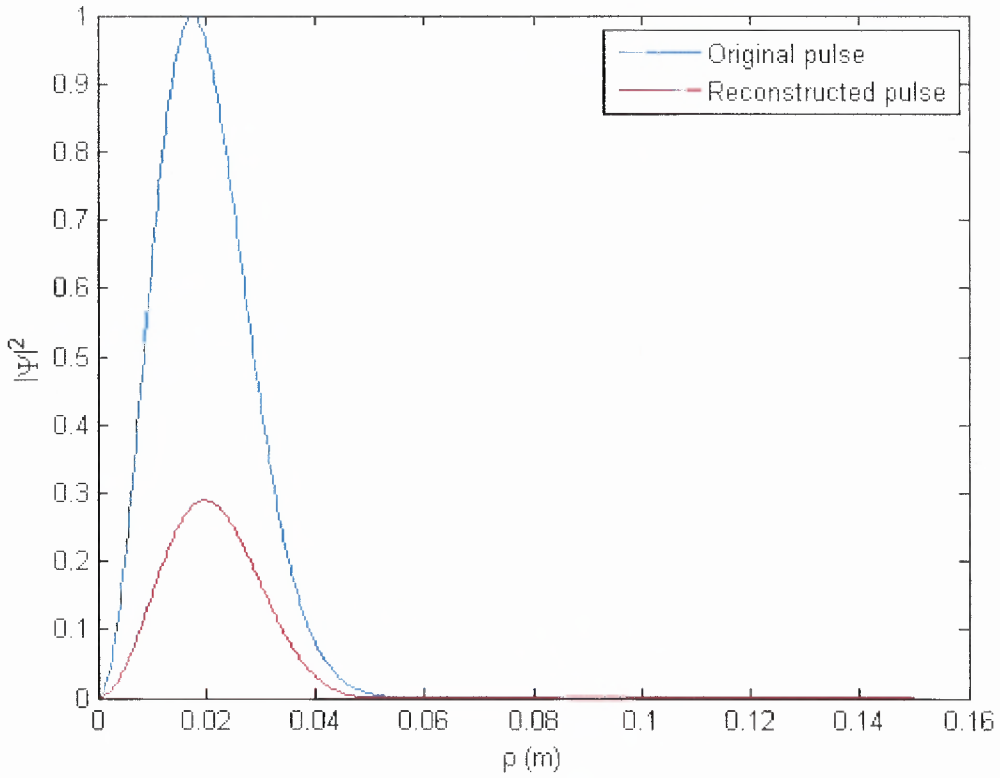

Figure 4.23 Comparison of the intensity profiles of the original and reconstructed pulses for Configuration 1 pulse in the Example 2.

Figure 4.23 shows that the transverse localization of the pulse is preserved. The reconstructed pulse suffers greatly from power loss and this is due to the strong presence of backward traveling components in its spectrum, which could not be generated using this approach and accordingly contribute to the lower power efficiency.

To demonstrate the time localization of the reconstructed pulse, the time profiles of both the original and the reconstructed pulses are compared in Figure 4.24.

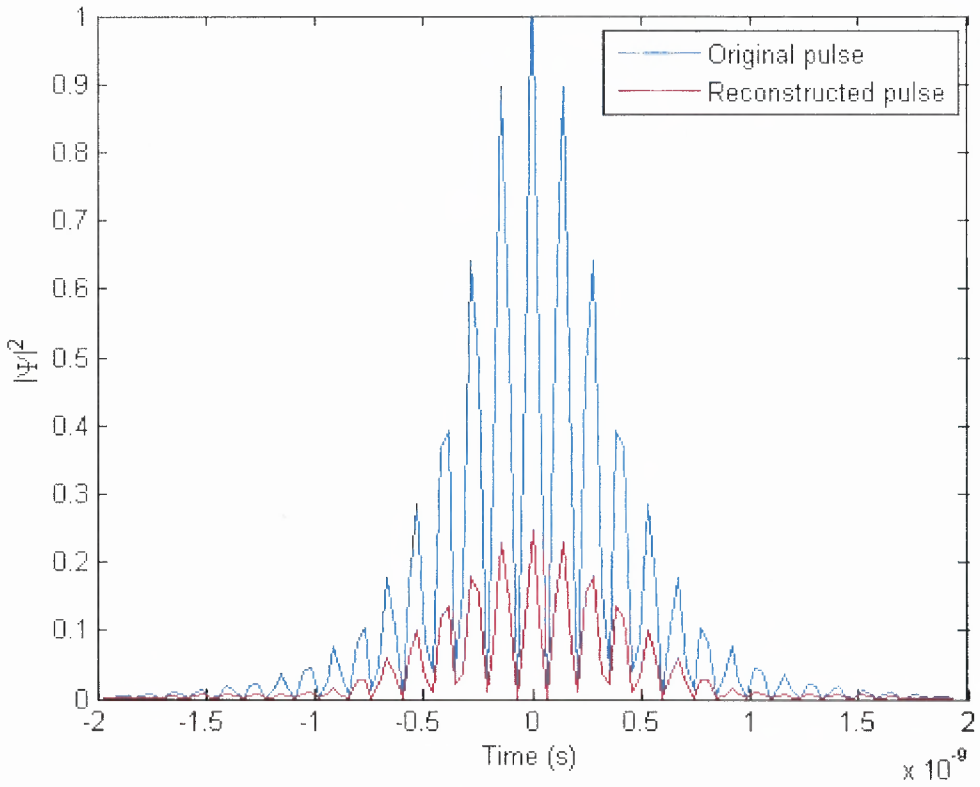

Figure 4.24 Comparison of the time profile of the intensities of the original and reconstructed pulses for Configuration 1 in the Example 2.

4.2.3 Excitation Configuration 2

The second excitation configuration uses only the first four modes of the waveguide and accordingly four current loops. No changes were made to either their locations or radii, and accordingly, their data is found in the first four rows of Table 4.4.

The corresponding currents as functions of time are shown in Figure 4.25, and their corresponding spectra are shown in Figure 4.26.

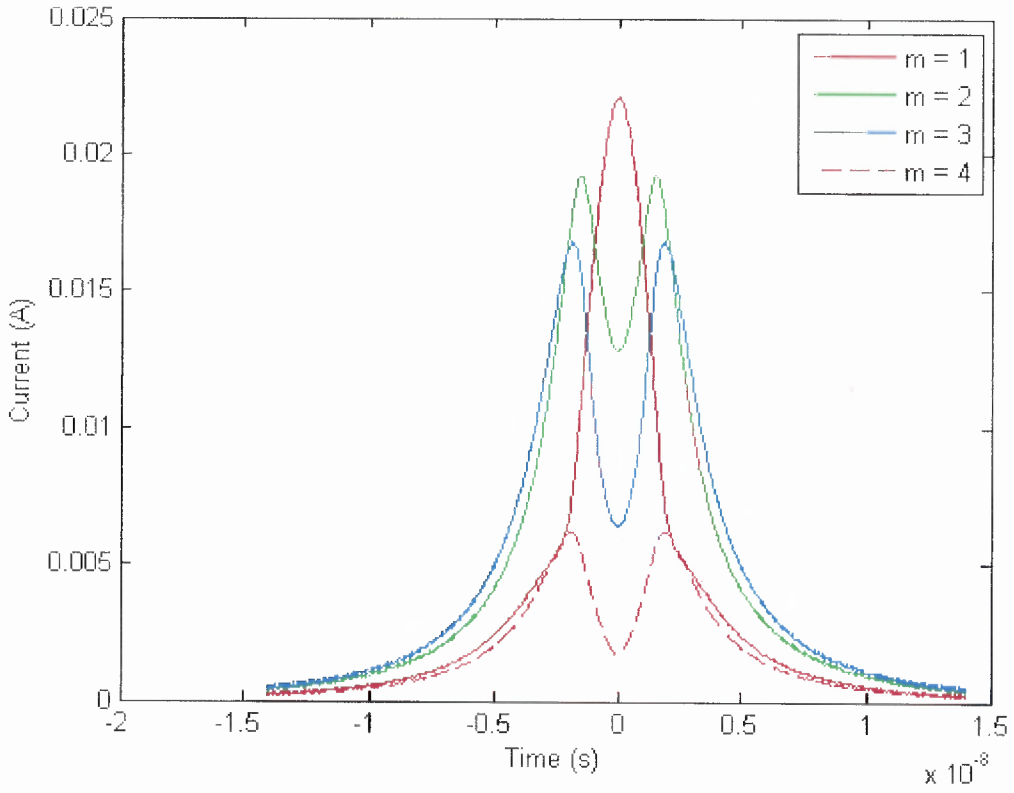

Figure 4.25 Excitation currents of configuration 2 pulse in the Example 2.

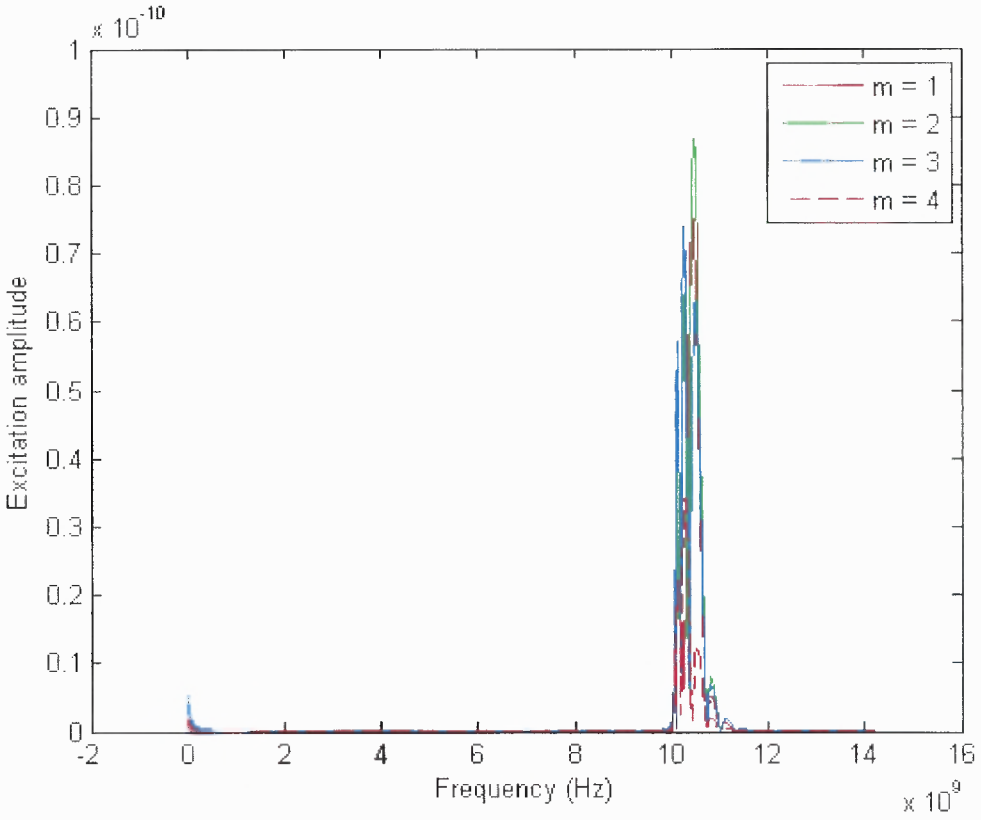

Figure 4.26 Spectra of the excitation currents of Configuration 2 pulse in the Example 2.

By solving the forward problem, the field of the reconstructed pulse is computed. Figure 4.27 shows the intensity profile comparison between the original and reconstructed pulse at the open end of the waveguide. The time profile of the intensities of both the original and reconstructed pulses is depicted in Figure 4.28.

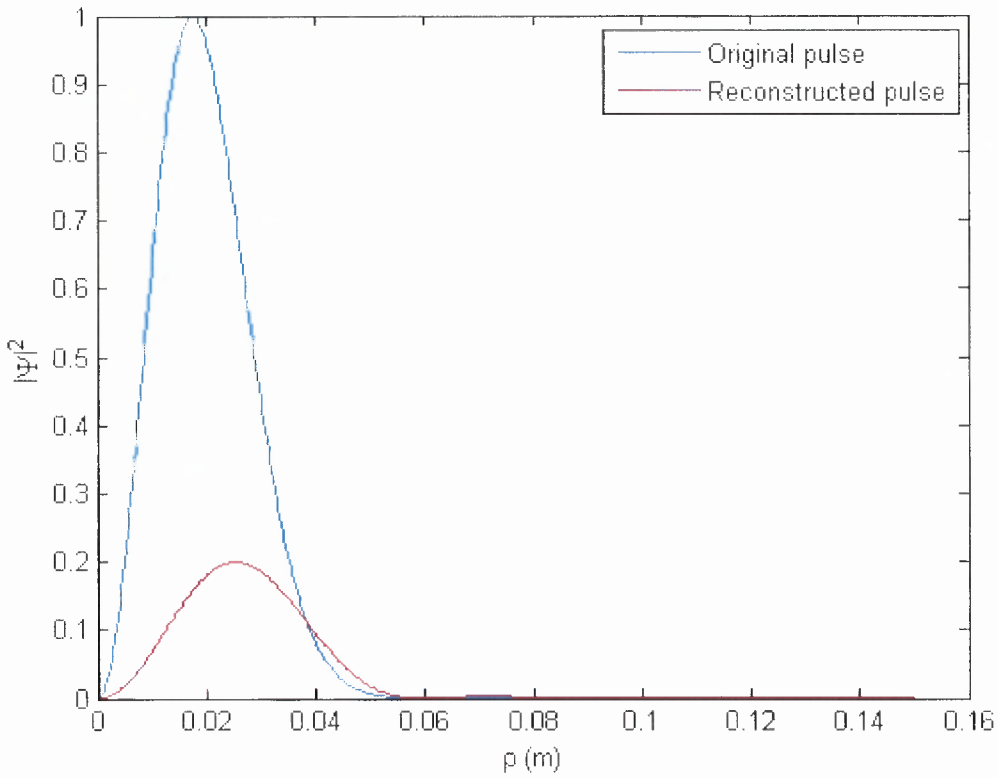

Figure 4.27 Comparison of the intensity profiles of the original and reconstructed pulses for Example pulse 2 using Configuration 2.

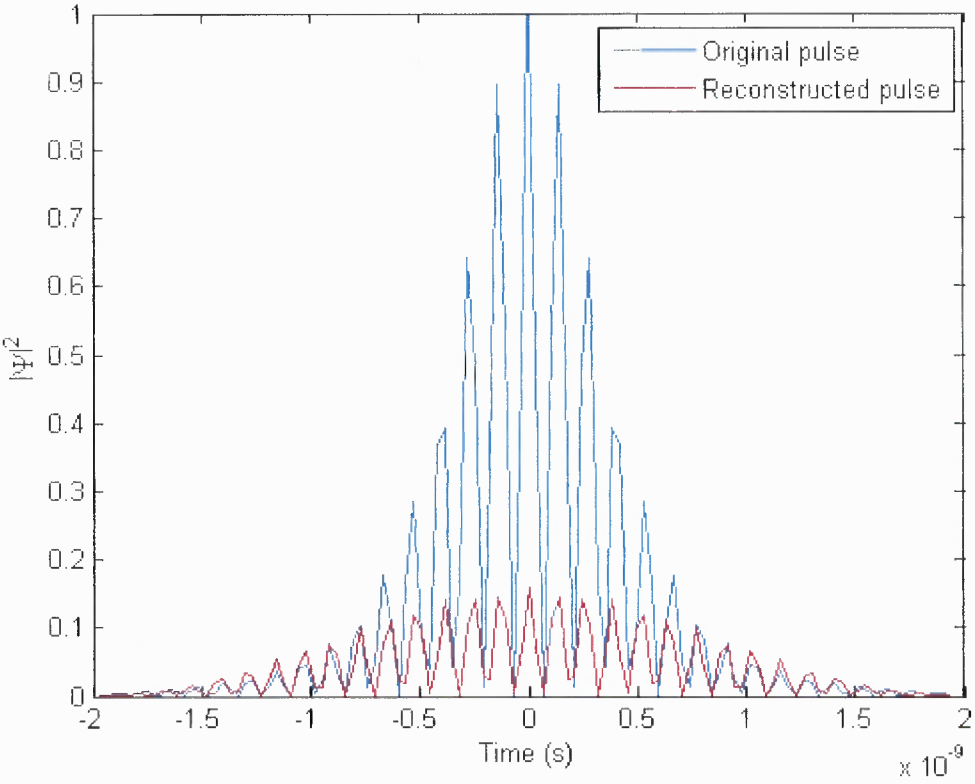

Figure 4.28 Comparison of the time profile of the intensities of the original and reconstructed pulses for Example 2 using Configuration 2.

While Figures 4.27 shows that the transverse localization is maintained in the reconstructed pulse, Figure 4.28 shows that the time profile exhibits delocalization and the pulse displays significant spread in time.

4.3.4 Accuracy and Efficiency

Following the same procedures as in sub-section 4.2.4, Table 4.5 lists the calculated accuracy and efficiency values for the Example 2 pulse generation techniques. For the rms error values, the amplitudes of the reconstructed pulses were normalized in order to make the accuracy calculation directly related to the pulse shape.

Table 4.5 Accuracy and efficiency of the excitation configurations for Example 2 pulse.

Configuration	**Accuracy (Δ_{rms})**	**Efficiency (γ)**
1	0.89%	21.9%
2	1.03%	19.4%

While the generated pulses are very low in efficiency, their profiles closely match the original pulses and this generation technique could be used in applications where high power efficiencies are not of a major concern.

CHAPTER 5

CONCLUSIONS AND FUTURE WORK

5.1 Conclusions

The study proposed a new technique for the generation of localized waves (LWs) based on the modal expansion method. In this study, the reconstructed pulse's full radial profile is presented and compared to the original pulse, hence avoiding one of the major shortcomings of the previously published studies of LWs generation techniques [13-16].

Using the modal expansion technique, localization of the pulse was maintained for greater distances than those previously reported. Although the profile of the reconstructed pulse was not exactly matching the original, but the transverse localization was well maintained.

The modal expansion technique is an efficient technique for the generation of TE MPS pulses. The calculated power efficiencies were high when the pulse's causality is maintained, while a significant drop in the output-to-input power was noted when a pulse with no strong causality is generated.

The flexibility in the choice of the number and order of the guided TE modes to represent the LW provides more freedom in determining the efficiency of the technique as the number and order of modes needed to generate the pulse could be tailored to the desired application.

The choice of the locations and radii of the current loops are important factors in determining the needed excitation function of the rings. By changing these parameters, different current shapes are obtained and accordingly, different reconstructed pulses.

To avoid power losses in the waveguide, the calculation of the excitation functions took into consideration the reflection from the closed end of the waveguide.

Overall, the modal expansion technique is a reliable and efficient technique for LWs generation. It can be easily tailored to realize a wide range of LWs.

5.2 Future Work

An important aspect is the generation of types of LWs other than the MPS pulse. The same derivation method of TE pulses can be applied to the FWM family of pulses, as they are subclasses of the MPS pulse. Investigation of the possible generation techniques of X-Waves is of great importance, as their transmission, reflection and scattering properties are intensively studied in the literature.

The practical realization of a LW launcher based on proposed method is of high importance and is currently being investigated. This realization requires additional investigation into different areas, such the non-linearity effects of the generation devices, heat deformation and mechanical stress of the waveguides and the error tolerance in the mechanical and electrical parts of the system.

As photonic crystals emerge fast into the scientific as well as the industrial arena, it is beneficial to study the possibility of using the modal expansion technique in generating LWs in photonic crystals in the optical regime. Materials with negative refractive index exhibit an inherent focusing nature and thus the possibility and feasibility of utilizing the focusing nature of these left-handed materials, as guiding media for the launcher, could be studied.

REFERENCES

1. J. N. Brittingham, "*Focus wave modes in homogeneous Maxwell equations: Transverse electric mode*," J. Appl. Phys. **54**, p. 1179 (1983).

2. T. T. Wu and R. W. P. King, "*Comments on focus wave modes in homogeneous Maxwell equations: Transverse electric mode*," J. Appl. Phys. **56**, p. 2587 (1984).

3. A. Sezginer, "*A general formulation of focus wave modes*," J. Appl. Phys. **57**, p. 678 (1985).

4. T. T. Wu and H. Lehmann, "*Spreading of electromagnetic pulses*," J. Appl. Phys. **58**, p. 2064 (1985).

5. R. W. Ziolkowski, "*Exact solutions of the wave equation with complex source locations*", J. Math. Phys. **26**, p. 861 (1985).

6. J. Y. Lu and J. F. Greenleaf, "*Nondiffracting X waves - exact solutions to free space scalar wave equation and their finite aperture realization*," IEEE Trans. Ultrason. Ferroelec. Freq. Contr. **39**, p. 19 (1992).

7. P. Hillion, "*Splash wave modes in homogeneous Maxwell equations*," J. Electromagnetic Waves Appl. **2**, p. 725 (1988).

8. P. Hillion, "*Arrow wave modes*," J. Opt. A: Pure Appl. Opt. **3**, p. 311 (2001).

9. R. W. Ziolkowski, "*Localized wave physics and engineering*," Phys. Rev. A **44**, p. 3960 (1991).

10. R. W. Ziolkowski and D. K. Lewis, "*Verification of the localized wave transmission effect*", J. Appl. Phys. **68**, p. 6083 (1990).

11. D. Power, R. Donnelly and R. MacIsaac, "*Spherical scattering of superpositions of localized waves*", Phys. Rev. E **48**, p. 1410 (1993).

12. D. Mugnai, A. Ranfagni and R. Ruggeri, "*Observation of superluminal behaviors in wave propagation*," Phys. Rev. Lett. **84**, p. 4830 (2000).

13. P. Saari and K. Reivelt, "*Evidence of X-shaped propagation invariant localized light waves*," Phys. Rev. Lett. **79**, p. 4135 (1997).

14. K. Reivelt and P. Saari, "*Optical generation of focus wave modes*," J. Opt. Soc. Am. A **17**, p.1785 (2000).

15. C. Conti and S. Trillo, "*X waves generated at the second harmonic*," Opt. Lett. **28**(14), p. 1251 (2003).

16. A. M. Shaarawi and I. M. Besieris: "*On the Superluminal propagation of X-shaped localized waves*", J. Phys. A, **33**, pp.7227-7254 (2000).

17. A. M. Shaarawi and I. M. Besieris: "Relativistic causality and Superluminal signalling using X-shaped localized waves", J. Phys. A, **33**, pp.7255-7263 (2000).

18. I. M. Besieris, A. M. Shaarawi, R. W. Ziolkowski, "A bidirectional travelling plane wave representation of exact solutions of the scalar wave equation", J. Math. Phys., **30**, pp. 1254-1269 (1989).

19. M. Zamboni-Rached, E. Recami, H. E. Hernandez-Figueroa, "New localized Superluminal solutions to the wave equations-with finite total energies and arbitrary frequencies", European Physics Journal D, **21**, 217-228 (2002).

20. I. S. Gradshteyn and I. M. Ryzhik: Integrals, Series and Products, 4th edition (Acad. Press; New York, 1965).